# Extrusion-based 3D printing and characterisation of biodegradable porous iron-akermanite composite scaffolds

By

Karl Galea Naudi Borg

Student Number: 5058457

in partial fulfilment of the requirements for the degree of

**Master of Science**

in Biomedical Engineering

at the Delft University of Technology,

to be defended publicly on *Thursday, August 26, 2021, at 15:30.*

| | | |
|---|---|---|
| Supervisor: | Dr. Jie Zhou | |
| Thesis committee: | Dr. Peymen Taheri | TU Delft |
| | Niko Eka Putra, M.Sc. | TU Delft |

*This thesis is confidential and cannot be made public until* ***December 31, 2023.***

An electronic version of this thesis is available at http://repository.tudelft.nl/.

TU Delft

# Abstract

The increase in the average human lifespan and the higher prevalence of extreme sports communities in the current society has led to an unfortunate increase in bone defect and fracture cases. Consequently, there is a growing demand for bone fracture therapy and technology. In the case of orthopaedic implants, research has been gradually inclining towards designing biodegradable, biologically integrative porous scaffolds, capable of providing a healthy environment for optimal bone regeneration. Moreover, by mimicking the interconnected porous structures of the natural bone matrix, these implants allow the flow of blood, oxygen and nutrients that are essential in the healing and maintenance of healthy osseous tissue. The gradual dissolution of the structure deems it a non-permanent implant, ultimately completely replaced by natural bone tissue.

Pure Fe can offer suitable mechanical properties to support the applied loads of habitual human activities, however, it exhibits too slow biodegradation rates and fails to display satisfactory bone integrative characteristics. Fe-based bioceramic composites are reported to offer biocompatibility, biodegradation and mechanical properties ideal for bone substitution applications. Currently, additively manufactured (AM) Fe-bioceramic composites are one of the most promising material classes for biodegradable scaffold implants.

This thesis investigates the extrusion-based AM Fe-akermanite (5 to 15 vol%) composite scaffolds. The fabrication method involved 3D printing printable Fe-akermanite inks followed by heat treatment in an inert environment. Static *in vitro* immersion testing was conducted to evaluate the degradation characteristics of the scaffolds. Furthermore, the as-sintered and degraded scaffolds were subjected to uniaxial compression testing to determine how the mechanical properties vary as the scaffold degrades. Cytotoxicity evaluations of the scaffolds were also conducted in the form of indirect and direct preosteoblast seeding and culture procedures.

The addition of akermanite hastened the degradation rate, with the Fe-15 (vol%) akermanite scaffolds displaying the fastest degradation and most rapid formation of corrosion products containing bone-forming elements, *e.g.*, Ca and P. The yield strength of the scaffolds decreased with increased akermanite content however remained within a suitable range even after degradation. Furthermore, the akermanite addition did not induce a shift towards brittle-like material behaviour. The scaffolds containing 15 vol% akermanite displayed superior cytocompatibility with preosteoblast cells. Therefore, Fe-akermanite composites exhibit great potential for use in biodegradable orthopaedic scaffold applications, with Fe-15 (vol%) akermanite displaying the most promising results.

# Acknowledgements

The research work disclosed in this publication is funded by the Tertiary Education Scholarships Scheme.

I express my sincere gratitude towards my thesis supervisor Dr. Jie Zhou not solely for his expert guidance but also for his enthusiasm and dedication for my research and the engineering field in general. I also thank my daily supervisor Niko Eka Putra, M.Sc. for his intuitive advice and support throughout the progression of my research.

I would like to communicate my admiration towards the academics and technical staff of the Department of Biomaterials and Tissue Biomechanics who have provided the knowledge and assistance necessary to complete and excel with my studies. In particular, I acknowledge Dr Lidy Fratila-Apachitei and Sander Leeflang for their assistance and encouragement.

I also place special thanks towards my family and friends who helped me endure the long nights of hard work — placing significant appreciation towards my grandmother Sandra, mother Sarah and young brother Samuel-Frank for their seemingly unlimited patience and constant support.

# Table of Contents

# 1 Introduction

Bone tissue is a critical component for maintaining a resilient skeletal system, playing important roles in various body functions such as structural support and motion. Bone consists of two synergistic structures; the smooth and dense outer cortical layer and the porous cancellous (or trabecular) bone, a porous network of much lower mechanical properties than the outer cortical [1]. Within this porous network reside the blood vessels and bone marrow [1]. Natural bone is a composite material comprised of collagen and other proteins that have been calcified by apatite deposits. The mineralised tissue optimises stiffness and rigidity whilst retaining fracture resistance. Apatite is the general term denoting a group of calcium phosphate, where hydroxyapatite ($Ca_{10}(PO_4)_6OH_2$) is the most common apatite in natural bone [2].

Bone can also be classified as a dynamic tissue. The bone composition and structure efficiently culture various bone cells that in turn participate in the maintenance of the bone [3]. The turnover rates of the skeleton approach 100% per year for infants, which reduces to about 10% per year in late childhood and usually remains at this rate or decreases throughout life [4]. The bone turnover (or remodelling) is a cyclic process of bone tissue resorption and formation, without altering the overall shape or density of the bone [4]. Bone remodelling is a critical process in the healing of fractured bone tissue. However, bone loss through trauma or diseases that incurs non-unions or critical size bone defects that will not heal within the patient's lifespan necessitates external intervention to promote bone regeneration [5]. In such cases, bone plates or implants are frequently utilised to mechanically assist bone realignment and support loads during the bone healing phase. Considering no complications due to mismatch or rejection issues, the average healing period is within 6 – 12 months post-fracture [6].

The latest advancement for bone substitution is biodegradable materials. The role of these biodegradable implants is to provide mechanical support during the initial stage of bone healing, while gradually degrading as the healing bone can support more mechanical load. Ultimately, the implant will be completely resorbed and new healthy bone tissue will regrow in its place [7], [8]. The Fe-based biodegradable metals are one class of biodegradable materials that naturally degrade when in contact with the *in vivo* environment. Although Fe-based metals can biodegrade, pure Fe exhibits very slow biodegradation, poor bioactive characteristics and ferromagnetic properties [9], [10]. Accelerated biodegradation of Fe-based materials has been achieved through alloying [11], [12] and surface modification [10]. However, the enhanced release of metallic ions due to more rapid biodegradation may be detrimental to the surrounding tissue and disrupt systemic health [6], [8]. Therefore, the biodegradation products of the implants must be composed of materials that are readily absorbed by the host metabolic systems. The rate of metal ion release is of importance for the biocompatibility of the implants. For example, even Fe ions that play important roles in human metabolic systems can cause unfavourable toxic effects if present above the tolerable limits [13].

In addition, Fe-based biodegradable metals are known for their higher mechanical strength compared to magnesium-based and zinc-based [6]. Orthopaedic implant materials that display exceedingly high mechanical modulus, relative to the bone tissue, may induce the stress-shielding effect, shielding the bone from the applied load. This phenomenon may lead to degraded implant-tissue adhesion and inflammation of the surrounding tissue which causes discomfort and pain that escalates until a revision surgery is required [14]. This challenge may be minimised with the inclusion of porosity and the consequent reduction in mechanical strength of the implant [15], [16]. Additionally, the incorporation of porous features, such as macro- and micropores, influence the degradation characteristics and cell responses [17]–[19]. The increase in surface area of the implant can improve biodegradation rates, promote cell adhesion and vascularisation of the forming bone [17], [19], [20]. Even though the implant functionality can be improved with intentional geometric design and material processing, Fe-based alloys still exhibit unfavourable bioactivity [6], [21], [22].

Compared to most metals, bioceramics offer superior biodegradation rates and bioactivity but are too brittle to be exclusively utilised as bone substitutes [23]. Combinations of brittle bioactive ceramics and ductile biodegradable Fe have been reported to enhance the biodegradation rate and bioactivity of the materials while providing suitable mechanical strength and ductility for bone substitution [17], [24]. In the recent years, Fe-based composites with the addition of calcium phosphate-based and silicon-based bioceramics have been researched, including hydroxyapatite (HA) [25]–[27], tricalcium phosphate (TCP) [17], [28], biphasic calcium phosphate (BCP) [27], magnesium silicide ($Mg_2Si$) [29], [30], calcium silicate ($CaSiO_3$) [31], [32] and bredigite ($Ca_7Mg(SiO_4)_4$) [21], [33].

When added into the bulk material, the bioceramic particles do not necessarily diffuse into the metallic crystal structure, as observed during metallic alloying, but rather form a material composed of multiple distinct phases. Different bioceramic concentrations in the Fe-based composites have been reported to alter the mechanical, biodegradation and biocompatible characteristics of the material [21], [27], [29], [33]. Currently, the most commonly explored fabrication technique is powder metallurgy (PM)-derived Fe-based composites, having been applied to Fe-$CaSiO_3$ [31], Fe-$Mg_2Si$ [29], Fe-HA [25], [27] and Fe-TCP [17], [27], [34]. PM techniques involve compacting powder material in a mould and subsequently consolidating by heat treatment. Overall, PM techniques are compatible with a wide range of materials and facilitate the generation of multi-material parts that contain complex 3D geometries.

In recent years, additive manufacturing (AM), namely, selective laser melting (SLM) [21], [33] and material extrusion [32], were also involved in the fabrication of Fe-bioceramic composites with the advantage of generating more intricate geometrical features and high flexibility in tuning the multi-material compositions. SLM has been utilised to produce Fe-bredigite ($Ca_7Mg(SiO_4)_4$) [33] and Fe-Pd-bredigite [21] composites, both of which have observed improved biodegradation and biocompatibility characteristics. SLM involves the selective melting of the powder material with a high energy source,

such as laser or electron beam [35], [36]. Though, the localised heating and material evaporation is known to induce embrittlement and generate voids. The material extrusion principle relies on incorporating an adhesive into the powder feedstock and thus allowing the layer-wise printing of a green component which is then combusted off during subsequent heat treatment [35]. The sintering process more closely approximates uniform thermal stress over the entire part when compared to the localised heating methods of other AM processes. Consequently, little or no residual stress is imparted into the final part. However, the green parts undergo structural shrinkage as an effect of the sintering process and need to be compensated for in the implant design [9], [32], [37]. To date, only Fe-$CaSiO_3$ composites have been derived through material extrusion AM [32]. The ability to incorporate macropores and random micropore features and the feasibility to tune multi-material compositions suggest that extrusion-based AM has a good prospect for the scaffold fabrication intended for bone substitutions.

With respect to bioceramics selection criteria, silicate-based bioceramics are shown to improve bone mineralisation [21], [31], [33]. Additionally, Ca- and Mg-containing silicates promise to further enhance cell proliferation by increasing the local availability of bone-forming ions [38]. The most prominent Ca-Mg-silicate bioceramics in the available literature include diopside ($CaMgSi_2O_6$), bredigite ($Ca_7MgSi_4O_{16}$) and akermanite ($Ca_2MgSi_2O_7$) [21], [33], [38], [39]. Out of the latter three bioceramics, diopside has been shown to degrade the most rapidly and display the highest osteoblast proliferation after 7 days [38]. However, the potential is present that diopside may be consumed too rapidly, consequently reducing the overall structural integrity of the scaffold and display little beneficial effect in long term biodegradable applications. Conversely, bredigite displays the slowest degradation rate and the poorest osteoblast proliferation rates [38]. Akermanite offers intermediate degradation rates and osteoconductive characteristics [38] (**Table 1**). Therefore, Fe-akermanite composites potentially offer the most suitable balance of enhanced degradation, cytocompatibility and mechanical stability throughout the application period.

Following the advances in Fe and bioceramic composites, this thesis aims to assess extrusion-based additively manufactured (AM) iron-akermanite composite scaffolds, intending to optimise fabrication parameters, characterise cellular response, biodegradation and mechanical characteristics, and identify the optimal material composition for biodegradative orthopaedic applications.

**Table 1** – Composition and Mass loss of Ca-Mg-Silicate bioceramics [38].

| | | ***Diopside*** | ***Akermanite*** | ***Bredigite*** |
|---|---|---|---|---|
| *Composition (wt%)* | Mg | 3.61 | 8.92 | 11.22 |
| | Ca | 41.67 | 29.40 | 18.51 |
| | Si | 16.69 | 20.60 | 25.94 |
| | O | 38.03 | 41.08 | 44.33 |
| *Mass Loss (%) (14 Days in Tris-HCL)* [38] | | 0.75 | 3.80 | 7.10 |

# 2 Materials and methods

## 2.1 Scaffold design and fabrication

This report investigated Fe-akermanite scaffolds produced via an extrusion-based AM technique. The fabrication procedure is based upon the investigation detailed in [9]. The Fe powder utilised was specified to 99.88% purity (Material Technology Innovations Co., Ltd., China) and sieved to a particle size of < 63 µm. The akermanite (AK) powder (Shanghai Institute of Ceramics, Chinese Academy of Sciences) was sieved to a nominal particle size of < 45 µm. The Fe and AK powders were then combined to form new powders of varying AK content (0, 5, 10 and 15 vol% AK). To ensure homogeneity, the powders were left to mix for 2 hr on a lab-built tumbler. The composite powders were then manually mixed with a 5 wt% aqueous solution of hydroxypropyl methylcellulose (HPMC) (Sigma Aldrich, Germany) to generate printable inks. The composite powder and HPMC concentrations of the printable inks are listed in **Table 2**. The rheological characteristics of the inks were analysed with an MCR302 rheometer (Anton Paar GmbH, Germany). A two-plate rotary setup was employed, varying the shear rate from 0.1 – 100 $s^{-1}$ and each test was performed in triplicate. Furthermore, the dissolution properties of AK were determined by mixing 4 ml of distilled water (equivalent to the volume of water in the ink) with the 0.6 g and 1.8 g of AK powder (equivalent mass of AK in the 5 and 15% inks). After 2 hr, mimicking the powder processing time, the solution was filtered using a 0.22 µm filter (Merck Millipore, Germany). The dissolved ions in the distilled water were quantified using an inductively coupled plasma optical emission spectroscope (ICP-OES, iCAP 6500 Duo, Thermo Scientific, USA).

The porous scaffold samples were designed using the GeSiM Robotics software (GeSiM Bio-instruments, Germany). The design encompassed a 10.5 mm height, 10 mm diameter, 410 µm strut width, 400 µm strut spacing, 328 µm layer thickness, 50% porosity and design surface area of 40.4 $cm^2$. The printable inks were extruded through a 410 µm nozzle utilising the 3D BioScaffolder 3.2 (GeSiM Bio-instruments, Germany), and the layer geometry was rotated by 90˚ between each layer (**Figure 1**). The printing velocity was 5 mm/s and the printing pressures of the various inks are listed in **Table 2**. The scaffolds were then heat-treated in the STF16/180 tube furnace (Carbolite Gero Ltd., UK) under an argon atmosphere. The two-stage heating cycle involved a debinding step at 350˚C for 1 hr (ramp of 2˚C/min) and a sintering step at 1200˚C for 6 hr (ramp of 4˚C/min) followed by natural cooling. The sintered samples were then stored within an argon environment until later use.

## 2.2 Macrostructure, cross-sectional, and porosity analysis

The shrinkage and mass loss imparted during sintering was determined by measuring the height, diameter and mass of the Fe-AK scaffold samples before and after heat treatment. Scanning electron microscopy (SEM) and energy-dispersive X-ray spectroscopy (EDS) were performed on the sample surface using the JSM-IT100 SEM (JEOL, Japan). The average strut width was calculated based on the SEM images. To characterise the cross-section, the samples were progressively ground to a 4000-grit

surface finish in isopropyl alcohol on a Struers Labopol-21 rotary grinding machine (Struers, Denmark). The cross-section was then observed using SEM and the solid fraction of the pores, AK and Fe were determined by threshold techniques with ImageJ (NIH, USA). The solid fraction [%] of the pores ($X_p$) and AK ($X_{AK}$) were calculated by the following equations:

$$X_p = \left(1 - \frac{Pore\ area}{Total\ area}\right) \times\ 100\% \quad \text{(Equation 1)}$$

$$X_{AK} = X_p - \left(\left(1 - \frac{AK\ \&\ pore\ area}{Total\ area}\right) \times\ 100\%\right) \quad \text{(Equation 2)}$$

The absolute porosity of the sintered scaffolds was calculated based on the mass and volume of the as-sintered samples as described by the following equation:

$$\varphi_a = \left(1 - \frac{m/p}{V_{bulk}}\right) \times 100\% \quad \text{(Equation 3)}$$

where $\varphi_a$ is the absolute porosity of the scaffold [%], m is the mass of the as-sintered scaffold [g], $V_{bulk}$ is the bulk volume of the scaffold [$cm^3$] and $\rho$ is the theoretical density of the Fe-AK composite [$g/cm^3$] (**Equation S1)**, refer to **Table 2**. Furthermore, the interconnected porosities were also evaluated based on the ASTM standard B963-13 [40]. This standard uses Archimedes' principle and employs the following equation:

$$\varphi_i = \left(\frac{\rho_e}{\rho_o} \times \frac{m_{ao} - m_a}{m_{ao} - m_{eo}}\right) \times\ 100\% \quad \text{(Equation 4)}$$

where $\varphi_i$ is the interconnected porosity [%], $\rho_e$ is the density of ethanol (0.8 $g/cm^3$), $\rho_o$ is the density of oil (0.9 $g/cm^3$), $m_a$ is the mass of the scaffold in air [g], and $m_{ao}$ and $m_{eo}$ are the masses of the scaffold impregnated in oil and ethanol, respectively [g].

## 2.3 X-ray diffraction phase analysis

The phase composition of the Fe and Fe-AK composite scaffolds was evaluated using the BrukerD8 Advance diffractometer Bragg-Brentano geometry and Lynxeye position sensitive detector (Bruker, USA). The scanning range varied between 20˚ - 100˚, with step size and time of 0.030˚ and 2 s, respectively. The machine was set up with a Cu Kα radiation source and a working voltage and current of 45 kV and 40 mA, respectively. The data was then evaluated with the Bruker software DiffracSuite.EVA vs 5.2 (Bruker, USA) and the International Centre for Diffraction Data PDF-4 database.

**Table 2.** Theoretical powder densities, binder volume and printing parameters.

| Sample | Theoretical density ($g/cm^3$) | HPMC (vol%) | Speed (mm/s) | Pressure (kPa) |
|---|---|---|---|---|
| *Fe* | 7.87 | 51.02 | 5 | 200 ± 5 |
| *Fe-5AK* | 7.62 | 52.55 | 5 | 175 ± 5 |
| *Fe-10AK* | 7.38 | 52.55 | 5 | 205 ± 5 |
| *Fe-15AK* | 7.13 | 52.55 | 5 | 235 ± 5 |

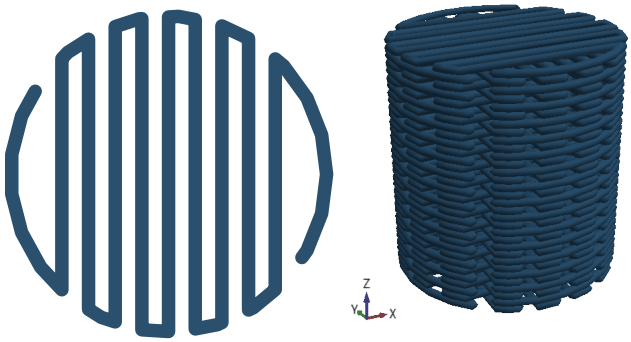

**Figure 1.** Graphical model of (left) layer geometry and (right) overall scaffold geometry.

## 2.4 Static *in vitro* immersion tests

The progression of *in vitro* corrosion was analysed by immersing the Fe and Fe-AK scaffolds in revised simulated body fluid (r-SBF), within a cell culture incubator (37˚C ± 0.5˚C, 95% relative humidity, and 5% $CO_2$). The r-SBF was prepared based on the composition listed in [41]. The solution volume-to-surface area ratio was 6.7 $mL/cm^2$. The samples were sterilised and the r-SBF was filtered (0.22 µm filter Merck Millipore, Germany) before commencing the static immersion and all tests were performed in triplicate. The immersion time points included; 4 hr, 8 hr, 1, 7 and 14 days. The concentrations of ionic release were measured after each time point employing inductively coupled plasma optical emission spectroscopy (ICP-OES, iCAP 6500 Duo, Thermo Scientific, USA). The mass loss induced by biodegradation was measured after cleaning in 50 vol% HCl solution (Sigma Aldrich, Germany) containing 3.5 g/L hexamethylenetetramine (Sigma Aldrich, Germany) for 10 min, proceeded by ultrasonic cleaning in isopropyl alcohol for 15 min, per the ASTM standard G1-03 [42]. The average corrosion rate was then evaluated based on the ASTM standard G31-72 [43], calculated by the following equation:

$$CR_{immersion} = 8.76 \times 10^4 \times \frac{m}{A \times \rho \times t} \quad \text{(Equation 5)}$$

where $CR_{immersion}$ is the corrosion rate [mm/year], m is mass loss [g], A is the designed surface area of the scaffold [$cm^2$], $\rho$ is the theoretical density of the scaffold [$g/cm^3$] and t is the immersion time [h].

The phase analysis of the corrosion products, produced during *in vitro* immersion, were characterised utilising XRD (using the same parameters as detailed in Section 2.3). Furthermore, the

morphology and elemental composition of the corrosion products were determined with SEM and EDS (JSM-IT100 SEM, JEOL, Japan).

## 2.5 Uniaxial compression tests

The scaffolds samples retrieved after 1, 7 and 14 days of *in vitro* static immersion were subject to uniaxial compression testing under a 100 kN load cell at a crosshead speed of 3 mm/min (Instron universal testing machine ElectroPuls E10000, Germany). The results yielded stress-strain relations of the scaffold samples, from which the yield strength of the samples was obtained as per ISO standard 13314:2011 [44]. The yield strength was determined by plotting a line parallel to the linear elastic region of the stress-strain curve, offset by 0.2% strain. The yield point is equal to the stress value at the intersection of the two plots. All tests were performed in triplicate.

## 2.6 Indirect cytotoxicity test

The indirect cytocompatibility of the Fe-AK scaffolds was evaluated through PrestoBlue assay (Thermo Fisher Scientific, USA). Extract media of each sample group was produced by immersing the samples in 8 mL (per sample) of α-MEM (without ascorbic acid, but with 10% FBS, 1% p/s) and incubating in a cell incubator for 3 days (37˚C ± 0.5˚C, 95% relative humidity, and 5% $CO_2$). MC3T3-E1 preosteoblasts (1 x $10^4$ cells) were then cultured in 200 µL of 100%, 75%, 50% and 25% dilutions of the extract media in a 48-well plate. A negative control group consisting of MC3T3-E1 preosteoblasts (1 x $10^4$ cells) were cultured in 200 µL of fresh α-MEM (without ascorbic acid, but with 10% FBS, 1% p/s). Additionally, a positive control group was also implemented containing solely α-MEM (without ascorbic acid, but with 10% FBS, 1% p/s). The culture medium was replaced after 1, 3 and 7 days. At each time point, 20 µL of PrestoBlue reagents were added to the wells and incubated at 37˚C for 1 hr. Subsequently, the media was transferred to a 96-well plate and the absorbance values at 530-590 nm wavelength were recorded with a Victor X3 Wallac plate reader (PerkinElmer, USA). The metabolic activity [%] was calculated by the following equation:

$$Metabolic\ Activity = \frac{Absorbance_{specimen} - Absorbance_{pos\ control}}{Absorbance_{neg\ control} - Absorbance_{pos\ control}} \times 100\% \qquad \text{(Equation 6)}$$

where the absorbance values of the positive control were deducted from both the specimen and negative control absorbance values prior to calculating the metabolic activity.

## 2.7 Direct cytotoxicity tests

Trypan blue cell counting assay tests were performed to evaluate the direct cytocompatibility of the samples. MC3T3-E1 preosteoblasts (4 x $10^4$ cells) were directly cultured on the scaffold samples (9.75 mm diameter and 2.05 mm height) and immersed in 8 mL of α-MEM (without ascorbic acid, but with 10% FBS, 1% p/s). The cells were trypsinised from the scaffold and well after 1, 7 and 14 d. A 10 µL of the cell suspension was then mixed with 10 µL of trypan blue dye (Bio-Rad, USA), transferred

to a dual-chamber cell counting slide and the number of cells was recorded with an automated cell counter (TC20, Bio-Rad, USA).

Furthermore, live/dead staining was performed to assess the distribution and morphology of the MC3T3-E1 cells (2 x $10^5$ cells) directly seeded on the scaffold samples (9.75 mm diameter and 2.05 mm height). After 1, 7 and 14 days, the samples were washed with PBS and immersed in PBS containing 2 µL/mL of calcein (Thermo Fisher Scientific, USA) and 1.5 µL/mL of ethidium homodimer-1 (Thermo Fisher Scientific, USA). The samples were then left for 30 min at room temperature in the dark. Subsequently, a fluorescence microscope (ZOE cell imager, Bio-Rad, USA) was used to image the live and dead cells on the Fe and Fe-AK scaffolds. SEM imaging of the cell morphologies was also performed. The cells were fixed to the scaffold surface with 4% formaldehyde (Sigma Aldrich, Germany) for 10 min, dehydrated in 70 and 100% ethanol (10 mins each) and preserved in hexamethyldisilazane (Sigma Aldrich, Germany) for 30 mins. The specimens were then allowed to dry before SEM imaging.

## 2.8 Statistical analysis

The mean ± standard deviation is presented for all values in this report. The indirect PrestoBlue assay results and direct cytocompatibility cell count comprise a two-way ANOVA statistical analysis followed by a Tukey *post hoc* test.

# 3 Results

## 3.1 Microstructure, sample mass and porosity

The microstructure of the printed Fe scaffolds was composed of a uniform distribution of Fe particles coated in the polymeric binder (**Figure 2a**). The Fe-AK scaffold samples comprised a similar microstructure however with AK particles uniformly distributed throughout the volume of the material (**Figure 2b-d**). Furthermore, the morphology of the Fe particles was smooth and more spherical when compared to the rough and fragmented AK particles. The bond between the powder and binder was strong enough to permit the printing of high aspect ratio scaffolds that effectively retained the printed geometry without distortion or buckling, refer to **Figure S1**. The average as-printed strut width of all sample groups was 412 ± 7 µm.

The viscosity of the Fe-AK inks increased with higher AK content, as shown in **Figure 3a**. The viscosity of the pure Fe ink fell between the Fe-5AK and Fe-10AK inks. Furthermore, ICP-OES analysis of the AK dissolution confirmed the solubility of AK in distilled water (**Figure 3b**). Ca and Si were shown to preferentially dissolve into solution as well as Mg ions, albeit in lower concentrations, where 15% AK produced ion release concentrations of 28.82, 9.93 and 0.35 ppm, respectively.

The average masses of the printed and as-sintered Fe and Fe-AK scaffolds are tabulated in **Table 3**. The pure Fe scaffolds displayed the highest mass that incrementally decreased with higher AK content, where the as-sintered mass decreased from 1.80 g with pure Fe to 1.46 g with the Fe-15AK samples. The absolute porosity of the samples was observed to increase with AK content, from 68.91% displayed by pure Fe to 72.36% exhibited by Fe-15AK (**Figure 3c**). The mass loss and dimensional shrinkage were relatively consistent for all samples irrelevant to AK content, with the variations in the measurements falling within standard deviation.

The as-sintered samples comprised an average strut width of 402 ± 12 µm. The microstructure of the pure Fe scaffolds displayed a porous structure of fused Fe particles, with distinct necking of adjacent particles and no visible remnants of the binder (**Figure 4**). In addition, the Fe-AK scaffolds contained AK particles embedded within the Fe particle-matrix (**Figure 5 - 7**). XRD analysis indicated that only α-ferrite phase was present in the pure Fe scaffolds, and α-ferrite and akermanite phases were present in the Fe-AK scaffold samples, implying that no new phases were generated during processing and heat treatment (**Figure S2**). Furthermore, EDS mapping of the AK containing samples showed a fine distribution of Ca, Mg, Si and O over the entire surface of the Fe particles (**Figure 5c, 6c, 7c**).

The sample cross-sections consisted of a matrix of partially fused particles (**Figure 5e, 6e, 7e**). The porous area fraction increased with higher AK concentrations from 1.6 ± 2.2% with Fe-5AK to 5.5 ± 3.5% with Fe-15AK. Similarly, the area fraction of AK was also observed to increase with the higher AK concentrations (**Figure 3d**). The smaller AK particles were integrated and uniformly distributed along the cross-section. EDS-line analysis indicated interdiffusion between the Fe and AK particles

(**Figure 5f, 6f, 7f**), where Fe diffused into the AK particles and mainly Ca, Si and Mg from the AK diffused towards the adjacent Fe particles.

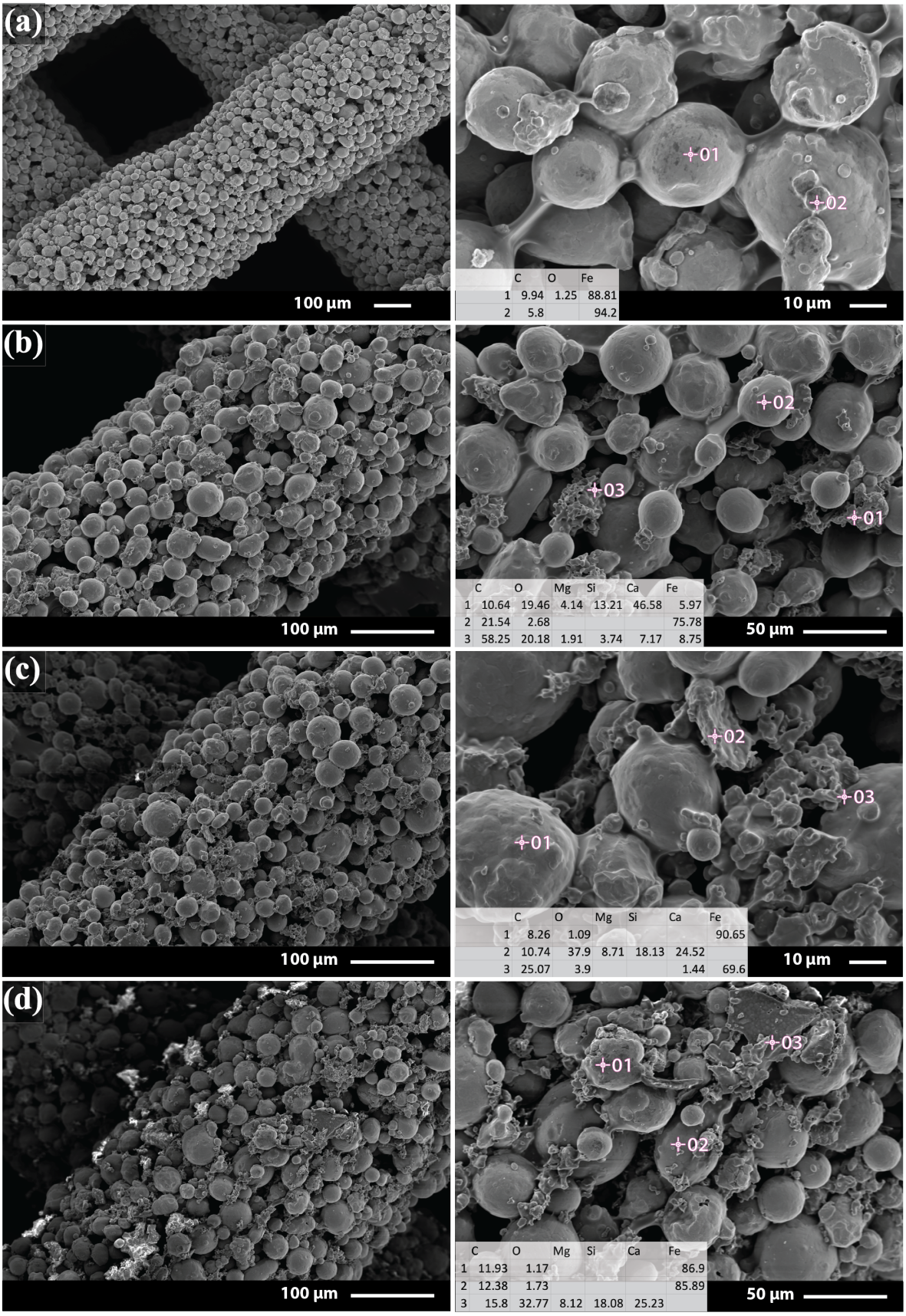

**Figure 2.** Microstructure of as-printed scaffolds (a) pure Fe, (b) Fe- 5AK, (c) Fe-10AK, (d) Fe-15AK.

**Table 3.** Scaffold mass and porosity measurements.

| ***Sample*** | | ***Pure Fe*** | ***Fe-5AK*** | ***Fe-10AK*** | ***Fe-15AK*** |
|---|---|---|---|---|---|
| *Printed mass (g)* | Average | 1.83 | 1.67 | 1.60 | 1.51 |
| | Std. Dev | 0.14 | 0.16 | 0.13 | 0.10 |
| *Sintered mass (g)* | Average | 1.80 | 1.64 | 1.57 | 1.46 |
| | Std. Dev | 0.12 | 2.70 | 0.16 | 0.09 |
| *Mass loss during heat treatment (%)* | Average | 1.56 | 0.89 | 2.08 | 1.80 |
| | Std. Dev | 2.36 | 0.27 | 3.26 | 1.77 |
| *Absolute porosity (%)* | Average | 68.91 | 70.76 | 71.68 | 72.36 |
| | Std. Dev | 1.64 | 2.70 | 2.80 | 1.75 |
| *Interconnected porosity (%)* | Average | 71.19 | 67.72 | 69.44 | 72.90 |
| | Std. Dev | 3.67 | 2.53 | 2.62 | 1.70 |
| *Diameter shrinkage (%)* | Average | 3.68 | 4.38 | 3.42 | 3.84 |
| | Std. Dev | 0.87 | 0.85 | 1.19 | 0.61 |
| *Height shrinkage (%)* | Average | 3.05 | 3.36 | 3.10 | 2.88 |
| | Std. Dev | 0.34 | 0.64 | 0.29 | 0.42 |

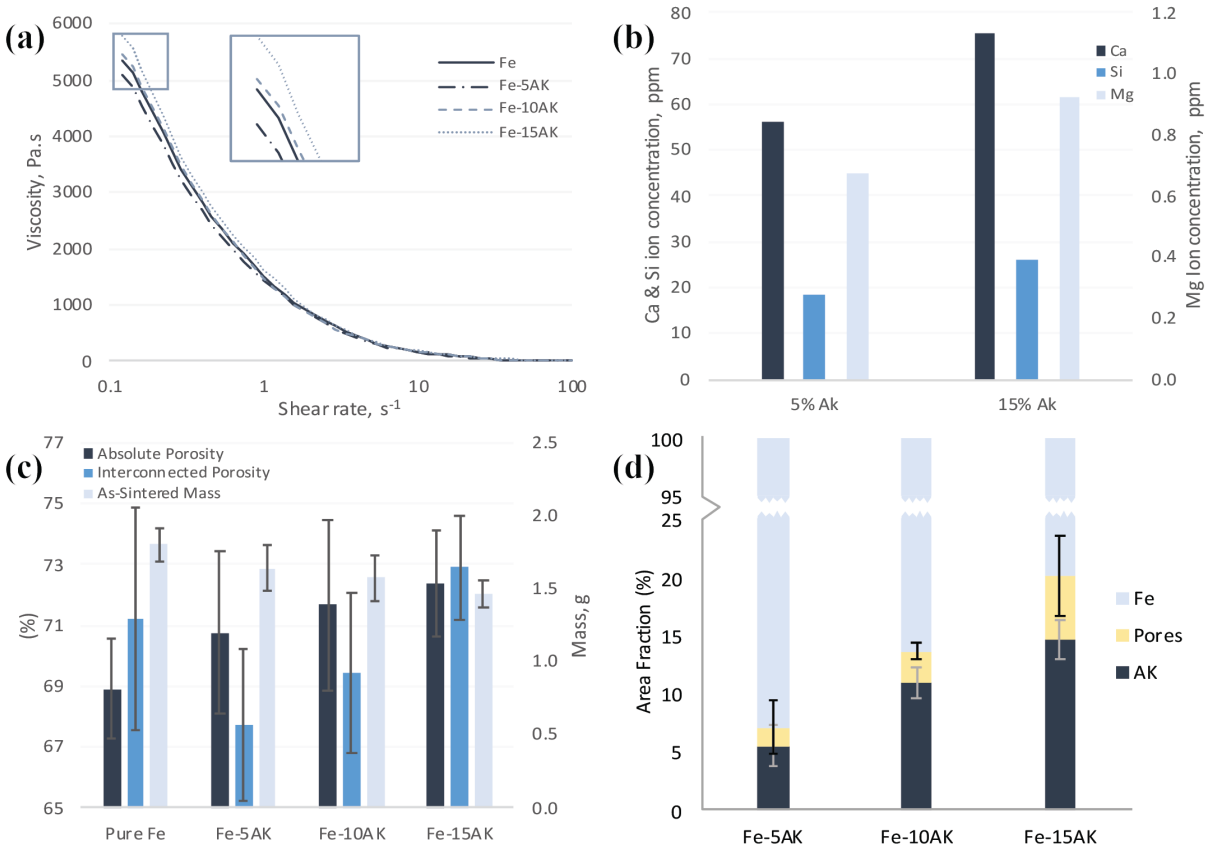

**Figure 3**. (a) Rheological evaluation of Fe and Fe-AK printable inks, (b) AK ion release in distilled water, (c) scaffold porosity and mass measurements and (d) area fraction of Fe-AK composite scaffolds.

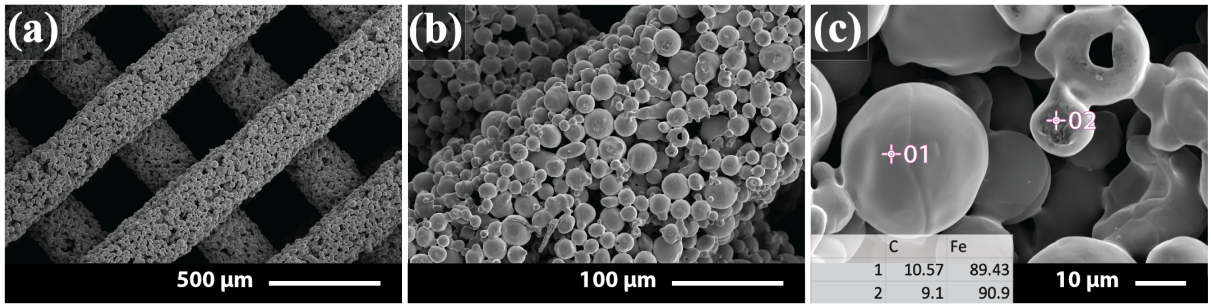


**Figure 4.** Microstructure of as-sintered pure Fe scaffold.

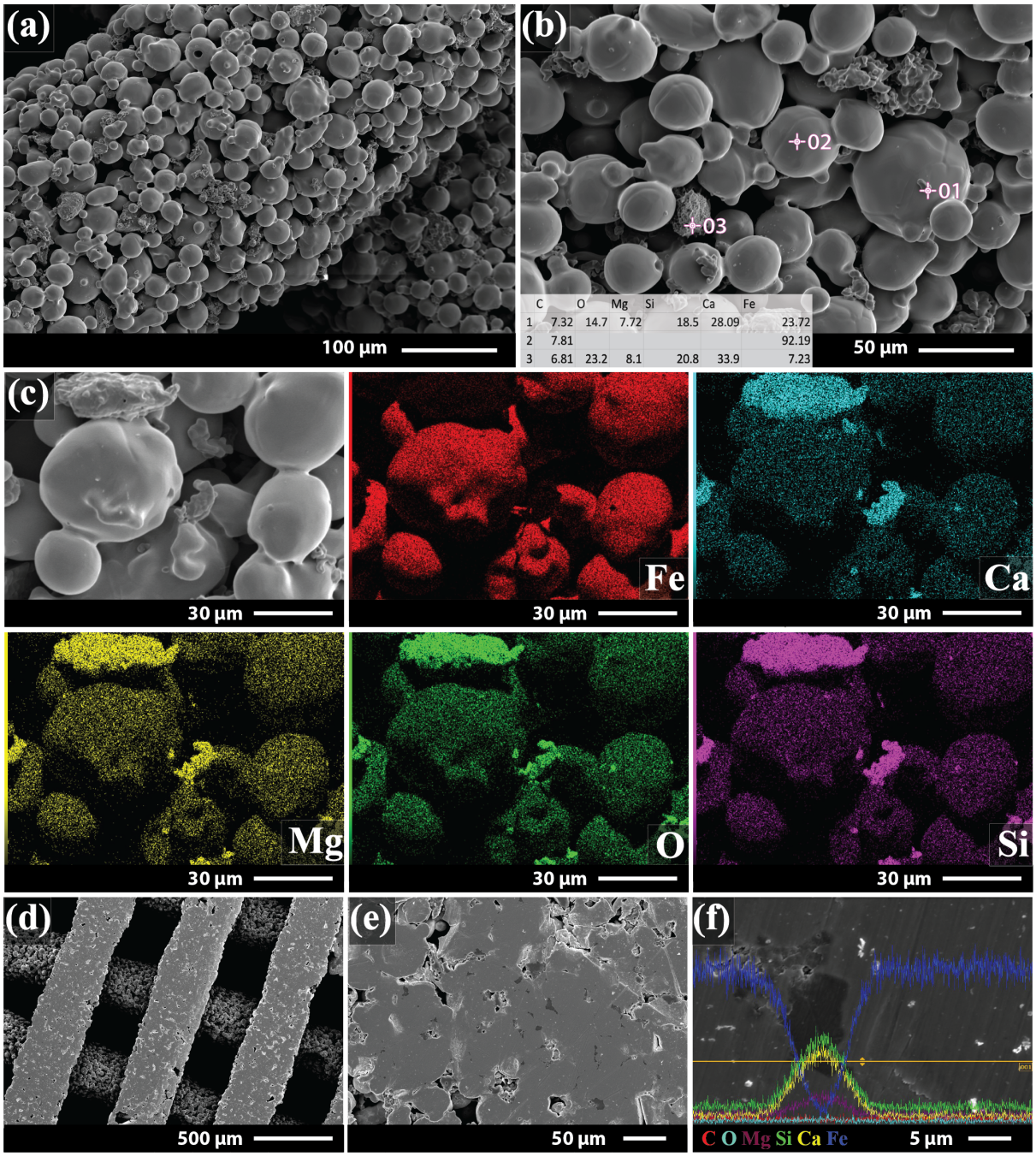

**Figure 5.** Microstructure of as-sintered Fe-5AK scaffold (a) low magnification image, (b) spot EDS measurement, (c) map EDS analysis, cross-sectional images (d) at lower magnification, (e) higher magnification and (f) line EDS measurement at Fe-AK interface.

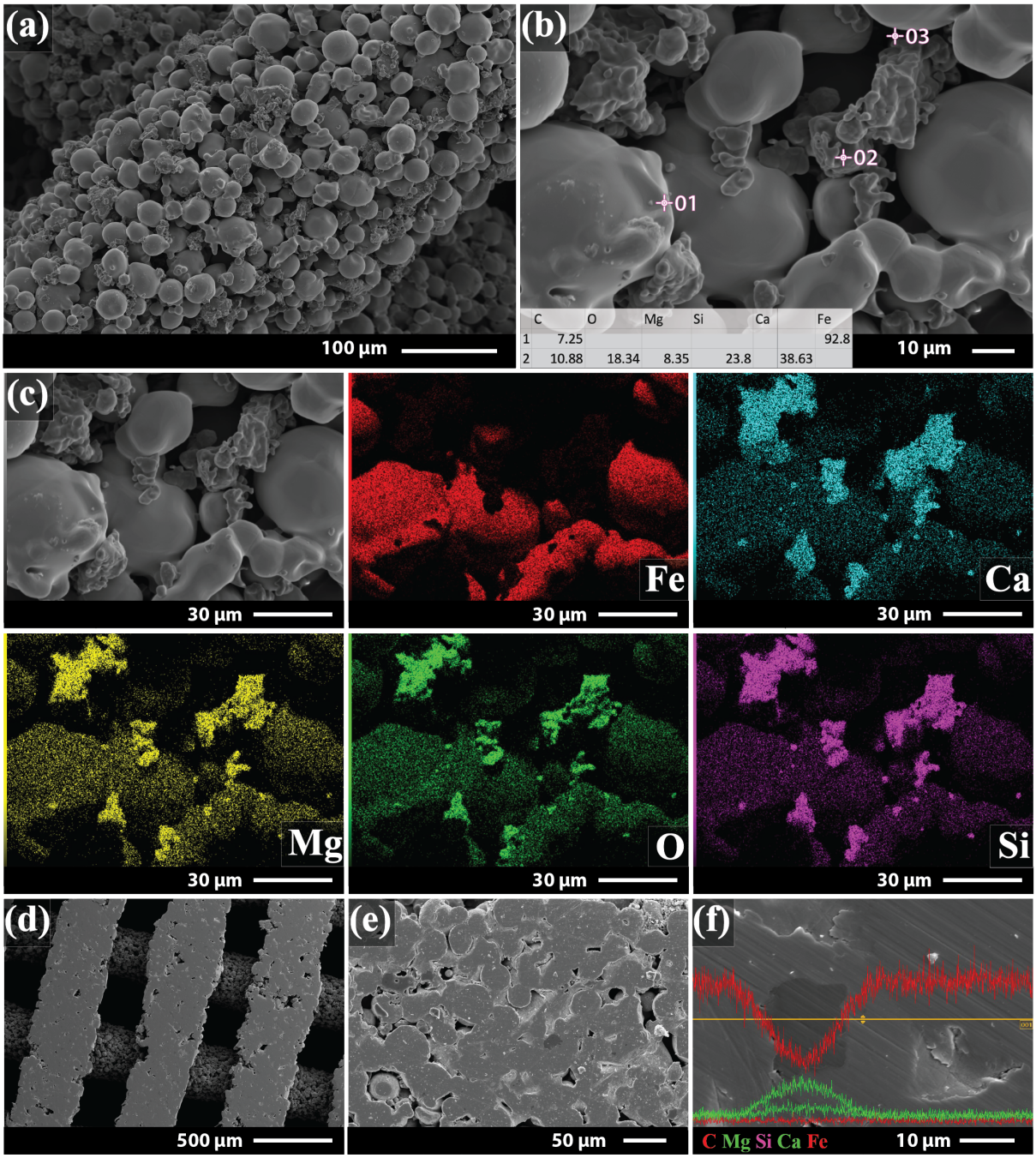


**Figure 6.** Microstructure of as-sintered Fe-10AK scaffold (a) low magnification image, (b) spot EDS measurement, (c) map EDS analysis, cross-sectional images (d) at lower magnification, (e) higher magnification and (f) line EDS measurement at Fe-AK interface.

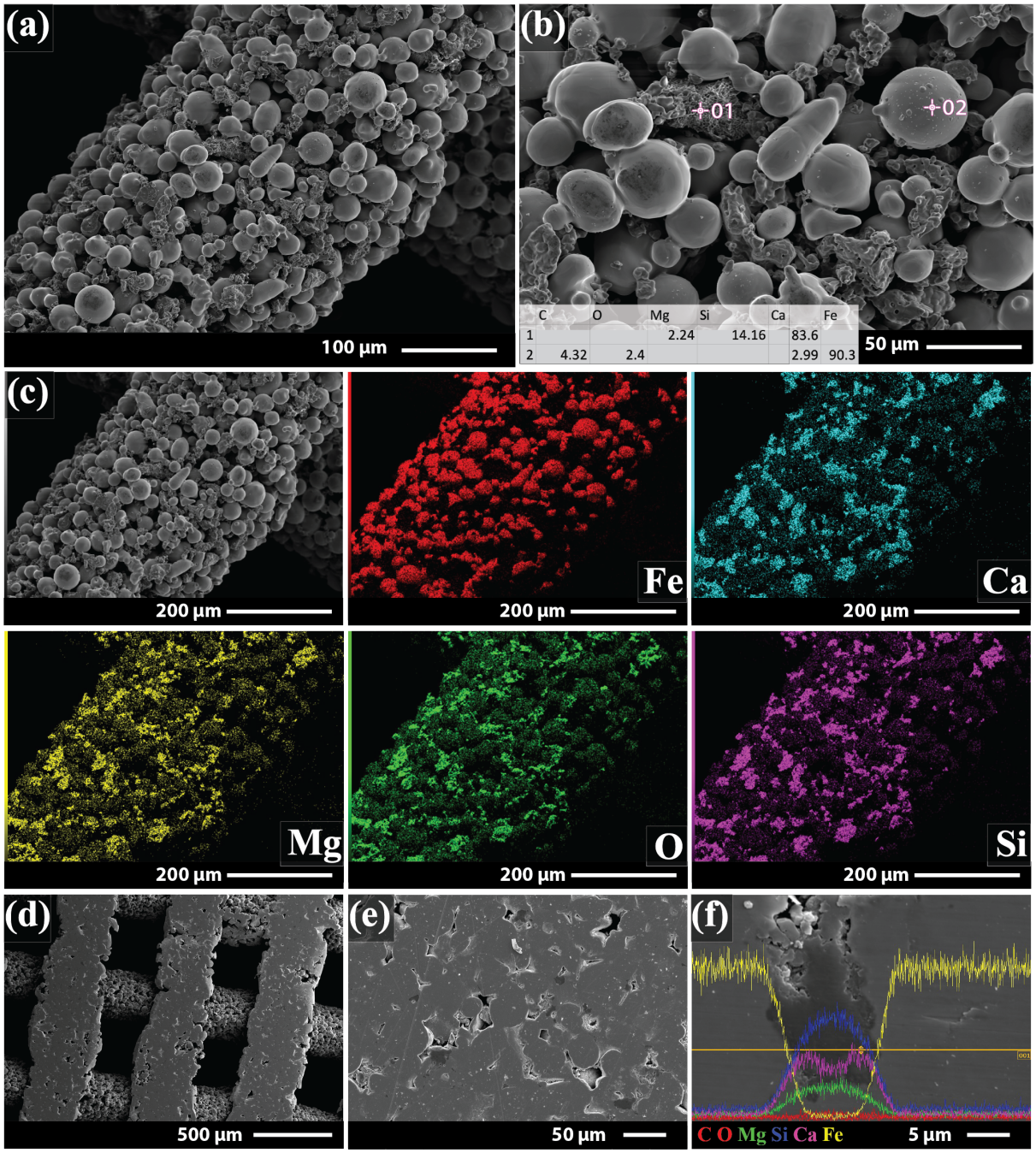


**Figure 7.** Microstructure of as-sintered Fe-15AK scaffold (a) low magnification image, (b) spot EDS measurement, (c) map EDS analysis, cross-sectional images (d) at lower magnification, (e) higher magnification and (f) line EDS measurement at Fe-AK interface.

## 3.2 Static *in-vitro* immersion tests

During the static immersion tests, the samples progressively developed a pale brown corrosion layer that was loosely bonded to the sample surface (**Figure S3**). Through XRD, the corrosion products were shown to be primarily lepidocrocite (γ-FeOOH) for all samples (**Figure S4)**. After 4 hr immersion, the beginnings of the corrosion layer was noted on all samples. With regard to the Fe samples, the morphology of the corrosion layer varied between a fine precipitate or relatively dense layer with numerous micro-cracks, both of which encompassed Fe-, C- and O-containing phases (**Figure 8a-b**). After 8 hr immersion, the Fe samples developed a more extensive corrosion layer that covered most of the exposed surfaces (**Figure 8c**). The morphologies of the corrosion layer resembled those present after 4 hr immersion, namely the dense layer with microcracking and the precipitated layer (**Figure 8d-e**). C- and O-containing rosette-like structures were also noted (**Figure 8f**). These structures progressively grew with the longer immersion times. By day 7, the precipitate structure developed into a globular surface which in certain areas had degraded further, forming a relatively rough surface of globules containing high porosity (**Figure 8g**). Ca, Na, K and P elements were detected on this rough and porous layer (**Figure 8g**). Additionally, needle-like structures containing Ca, Mg, Na, P and K also formed on the Fe scaffold surface (**Figure 8g**). After 14 days of immersion, the corrosion layer on the Fe samples further increased in volume, almost entirely bridging the inter-strut spacing (**Figure 8h**). The surface morphology principally comprised the rough and porous globular structure (**Figure 8h**). Additionally, a Cl-containing coral-like structure also formed during the 14-day immersion (**Figure 8i**)

For the AK-containing samples, the progressive degradation of the AK particles was clearly visible at the 4 hr timepoint (**Figure 9a, 10a, 11a**). Relative to the Fe scaffolds, the corrosion layer of the AK-containing samples was denser and formed in three distinct morphologies; a dense and rough corrosion layer (**Figure 9c**), a precipitate layer (**Figure 10a**), and globular structures encompassing micro and nano porosity (**Figure 11b**). With the Fe-5AK samples, Cl -containing rosette-like structures also formed on the scaffold surface (**Figure 9c**). After 4-hr immersion, AK particles were still detected on the scaffold surface (**Figure 9b**) however, by the 8-hr time point, no AK was detected on the surface of the samples, potentially completely dissolved in the immersion media or concealed by the newly formed corrosion layer (**Figure 9d, 10b 11c-d**). The Fe-10AK and Fe-15AK developed Ca-containing floral-like structures after 8 hr of immersion (**Figure 10b, 11d**).

After 1 day of immersion, the structures noted with the 8-hr immersion timepoint grew and became denser (**Figure 9d, 10c-d, 11c**). The Fe-10AK and Fe-15AK samples developed a corrosion layer of globular morphology containing principally Fe, Ca, C and O (**Figure 10f, 11e-f**). The Fe-5AK did not exhibit as aggressive corrosion at the day 1 time point, however, an extensive precipitation layer containing Fe, C and O was present (**Figure 9e-f**), more akin to the day 1 pure Fe samples. The overall coverage of the corrosion layer increased further with longer immersion times (**Figure 9g, 10e-f, 11g**). The inter-strut spacing was fully covered by day 14 (**Figure 9h, 10g, 11h**). With the Fe-AK composite

samples, the main morphologies observed was the degraded globular layer (**Figure 9i, 10h-i, 11i**). EDS analysis revealed that Ca was present on Fe-5AK, Fe-10AK and Fe-15AK (**Figure 9i, 10i, 11i**).

The EDS analysis indicated that by day 14, all samples groups developed Ca-, Na- and Cl-containing corrosion products. However, the Fe-10AK and Fe-15AK groups more rapidly developed Na- and Ca-containing phases, detectable after 8 hr of immersion. Where analogous corrosion products were noted on the Fe and Fe-5AK scaffolds after a 7-day immersion period. After cleaning, most of the corrosion layer was removed, revealing the underlying structure (**Figure S5**). Yet, certain corrosion products remained on the scaffold surface, namely Fe-, C- and O-containing phases (**Figure S5**). Moreover, mass loss measurements, recorded after cleaning, showed that the AK content is proportional to the degradation rate of the sample (**Table 4**). The degradation rate of the Fe-AK composite samples was relatively high after 1-day immersion but rapidly decreased with longer immersion timepoints. The Fe-15AK samples displayed the highest degradation rate of 0.17 mm/year after 14-day immersion. Whereas the pure Fe samples show the lowest degradation rate at 0.11 mm/year after 14-day immersion.

The results of ion release in the immersion media are graphically illustrated in **Figure 12**. With regard to the Fe-AK composite samples, Ca ions were present in the highest concentrations throughout immersion, between 97.62 and 104.69 ppm, only dipping with the Fe-5AK and Fe-10AK samples to approximately 90 ppm after 14 days. Ca ions also moved out of solution with the Fe samples, 68.7 ppm after 8 hr and diminished over immersion time. $PO_4$ ion concentration was relatively consistent and reduced over time for all samples. With the AK-containing samples, Mg and Si ion concentrations progressively increased with immersion time. Fe-15AK showed the highest concentrations, with Mg and Si increasing from 48.75 and 8.85 ppm after 8 hr to 57.80 and 20.38 ppm on day 14. Similarly, Fe ion concentrations increased with a longer immersion time, ranging between 0.28 ppm and 0.37 ppm after 14 days. Conversely, Si ion concentrations increased with immersion time, ranging between 14.15 and 20.38 ppm after 14 days, and were seemingly independent of AK content. The pure Fe samples displayed low Mg and negligible Si ion concentrations although relatively high Fe ion concentrations, increasing from 1.10 ppm to 3.97 ppm throughout the immersion period.

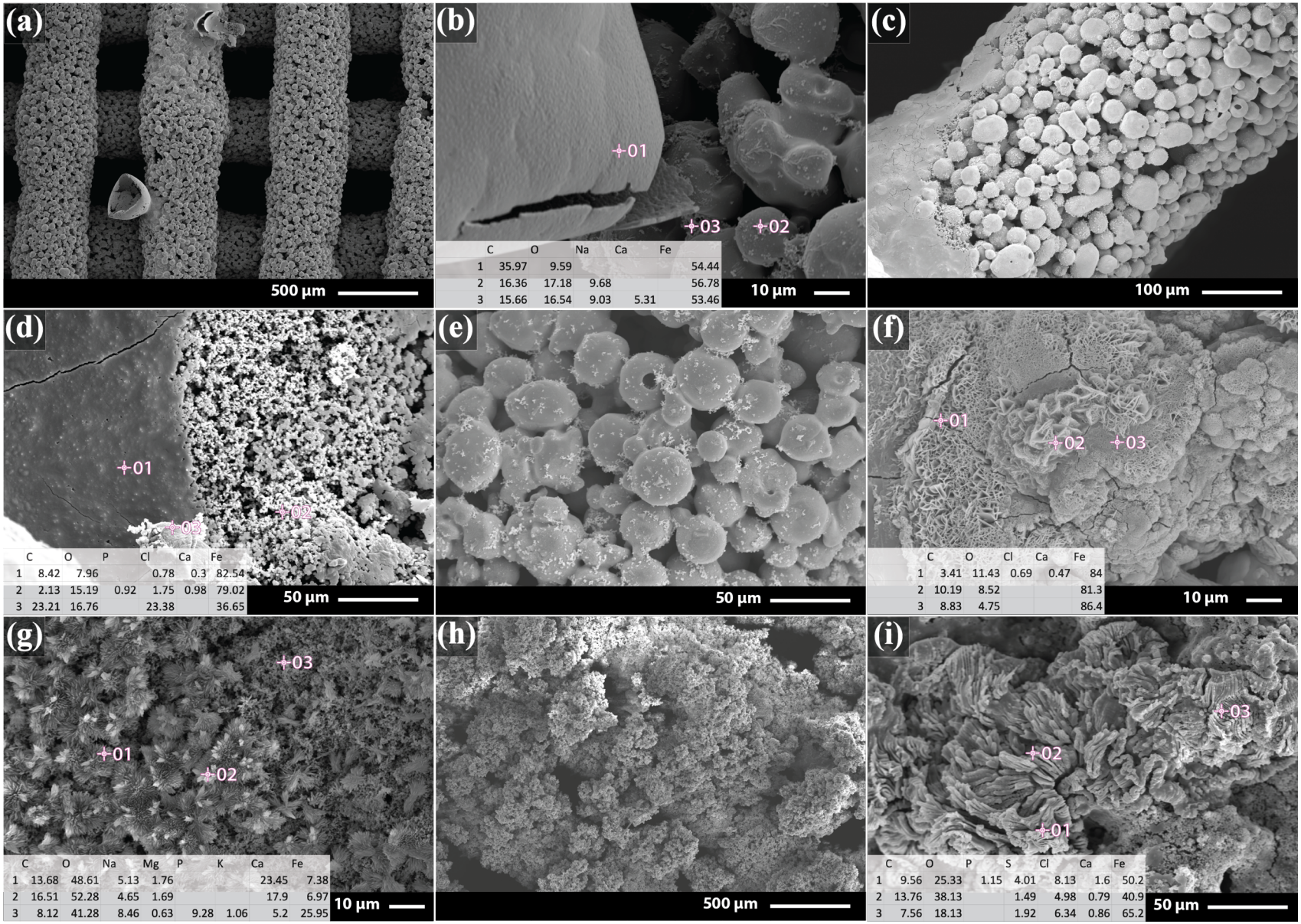


**Figure 8**. Morphology and chemical composition of Fe scaffolds biodegradation products after *in-vitro* degradation of (a, b) 4 hr, (c, d) 8 hr, (e, f) 1 day, (g) 7 day, (h, i) 14 day.

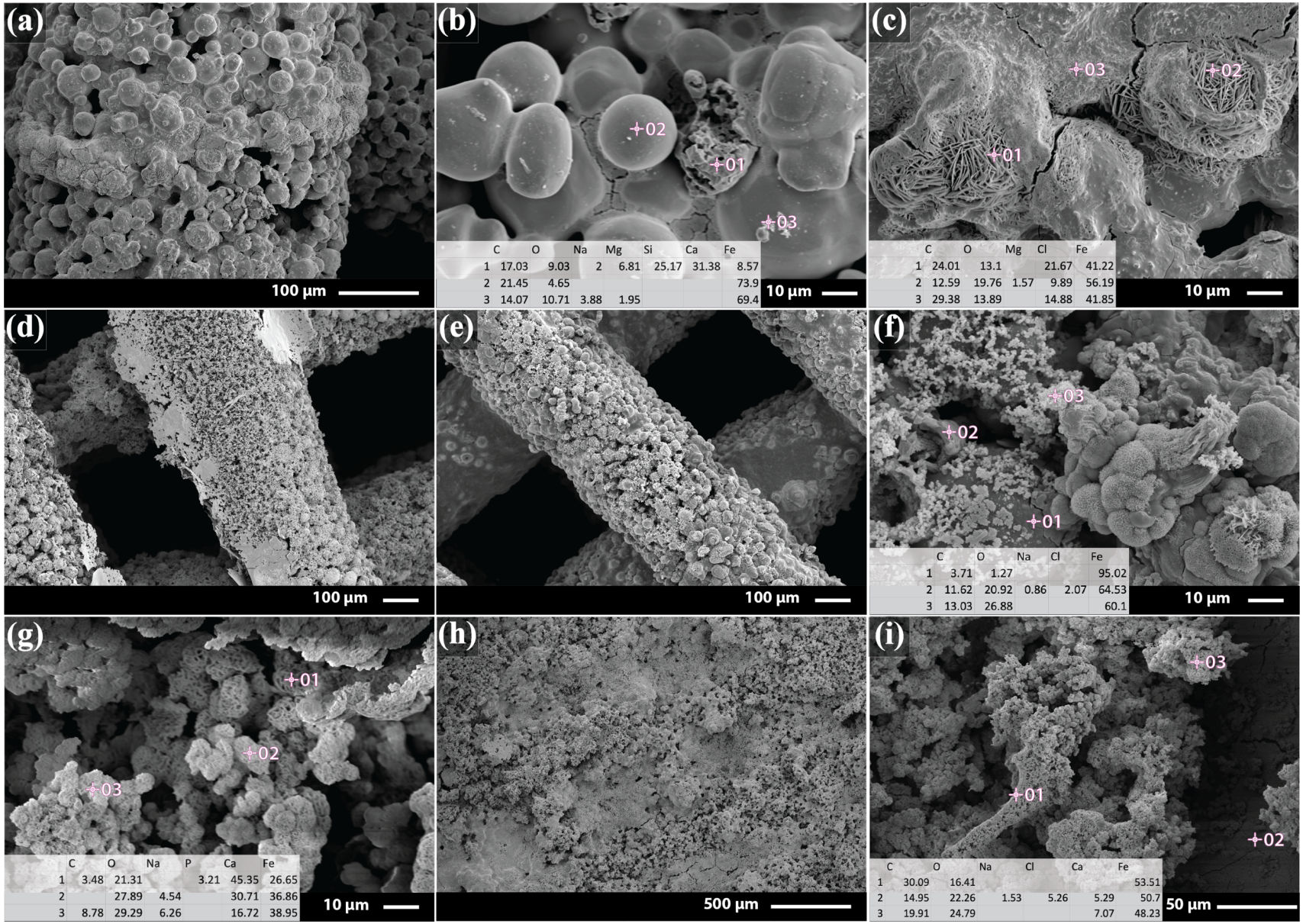


**Figure 9**. Morphology and chemical composition of Fe-5AK scaffolds biodegradation products after *in-vitro* degradation of (a, b, c) 4 hr, (d) 8 hr, (e, f) 1 day, (g) 7 day, (h, i) 14 day.

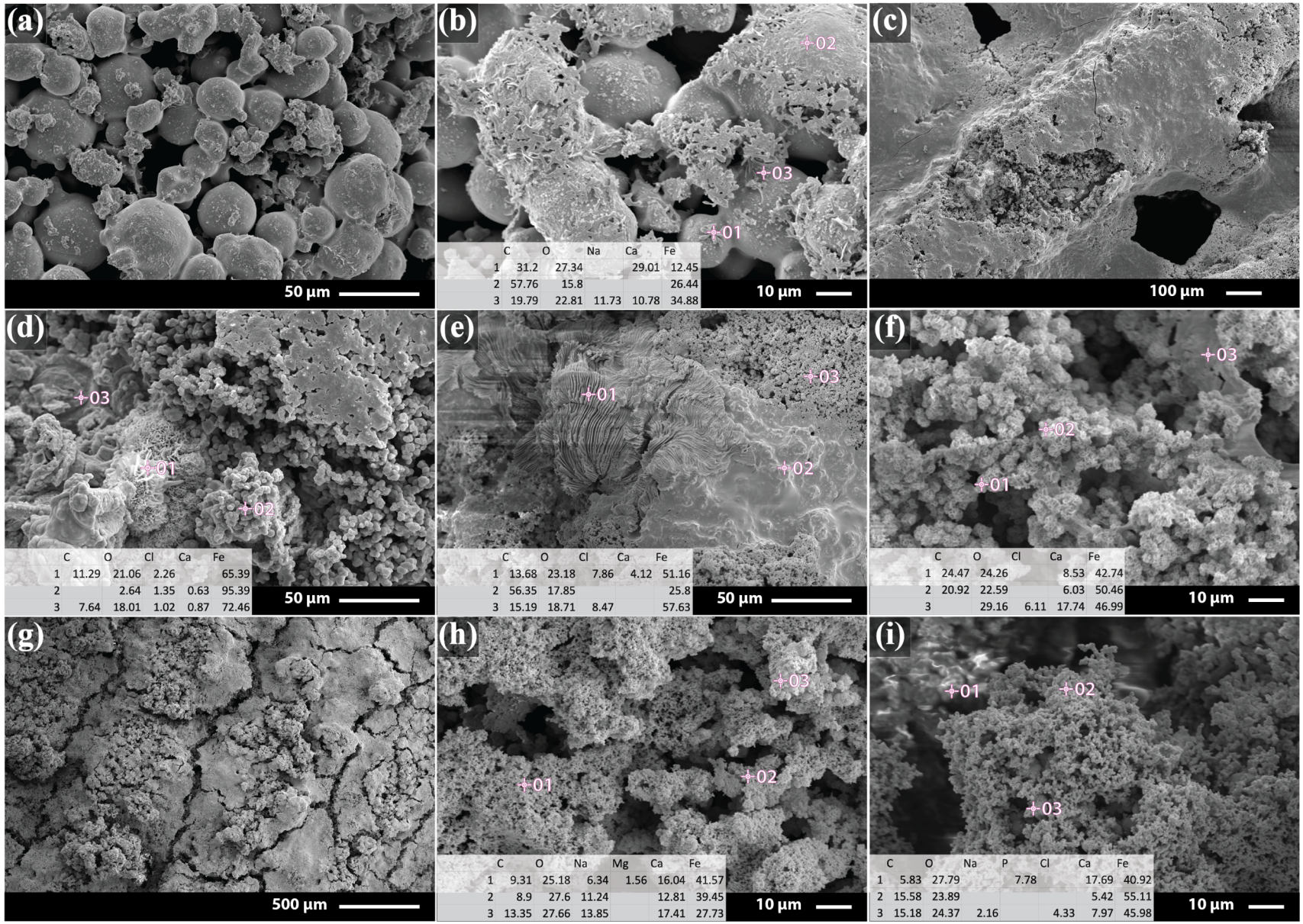


**Figure 10**. Morphology and chemical composition of Fe-10AK scaffolds biodegradation products after *in-vitro* degradation of (a) 4 hr, (b) 8 hr, (c, d) 1 day, (e, f) 7 day, (h, i) 14 day.

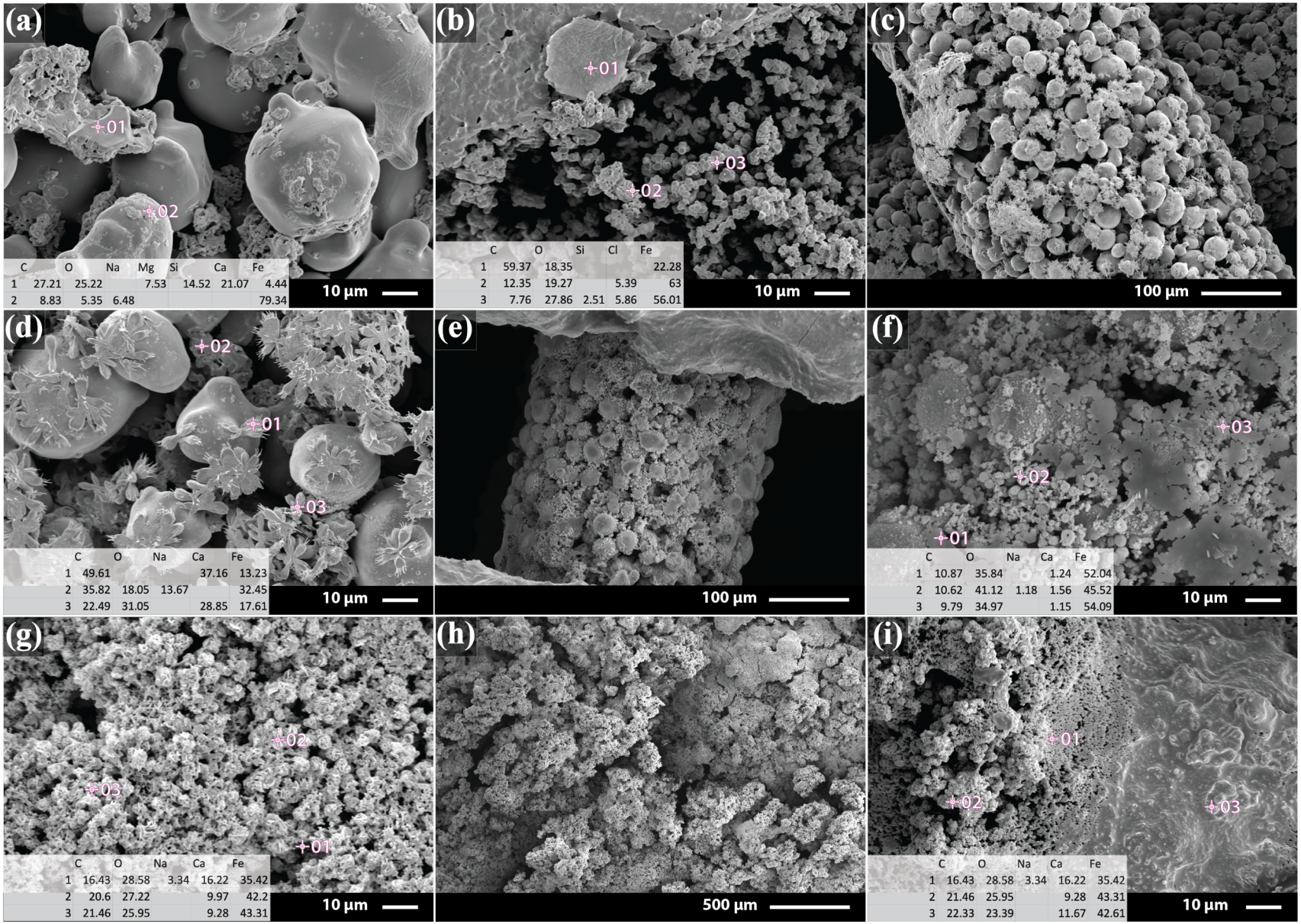


**Figure 11**. Morphology and chemical composition of Fe-15AK scaffolds biodegradation products after *in-vitro* degradation of (a, b) 4 hr, (c, d) 8 hr, (e, f) 1 day, (g) 7 day, (h, i) 14 day.

**Table 4**. Immersion mass loss results.

| | *Degradation Rates (mm/year)* | | | *Mass Loss (%)* |
|---|---|---|---|---|
| | *Day 1* | *Day 7* | *Day 14* | *Day 14* |
| *Pure Fe* | *0.64* | *0.22* | *0.11* | *7.6* |
| *Fe-5AK* | *2.11* | *0.19* | *0.12* | *8.7* |
| *Fe-10AK* | *3.80* | *0.23* | *0.14* | *10.3* |
| *Fe-15AK* | *3.76* | *0.32* | *0.17* | *12.4* |

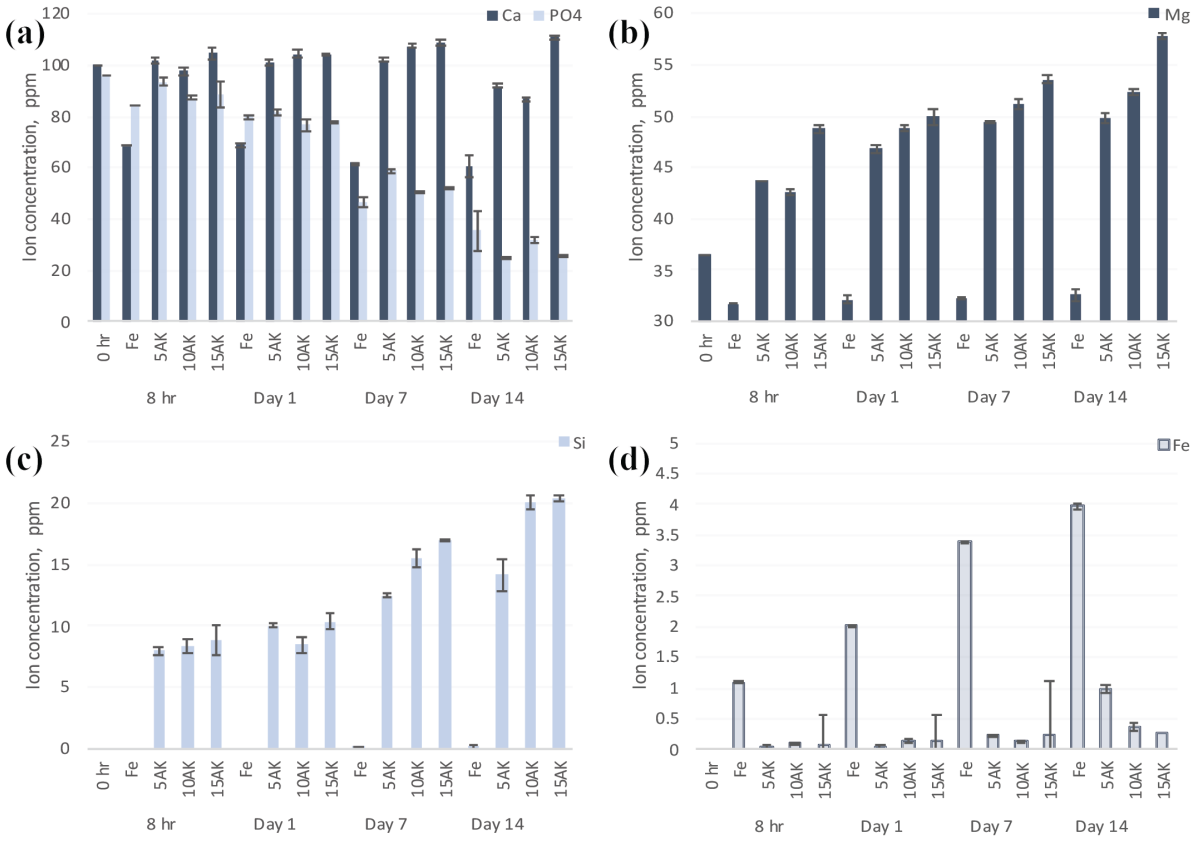


**Figure 12**. ICP-OES results of the immersion media after *in-vitro* degradation displaying (a) Ca and $PO_4$, (b) Mg, (c) Si and (d) Fe ion concentrations ('0 hr' measurements obtained from [41]).

## 3.3 Mechanical tests

Stress-strain curves of the Fe and Fe-AK scaffolds were derived from the uniaxial compression test results (**Figure 13a – d**). All samples initially displayed a linear elastic region followed by a plastic deformation phase, indicating ductile-like material behaviour. Moreover, all samples retained this ductile-like behaviour after in-vitro immersion. The as-sintered Fe scaffolds exhibited the highest yield strength of 7.15 ± 0.24 MPa. The measured yield strength of the as-sintered Fe-5AK, Fe-10AK and Fe-15AK composite scaffolds were 4.19 ± 0.24 MPa, 2.67 ± 0.08 MPa and 3.35 ± 0.40 MPa, respectively

(**Figure 13e**). Initially, *in vitro* immersion induced a relatively large decrease in compressive yield strength for all samples, with Fe and Fe-15AK scaffolds exhibiting 5.38 ± 0.29 MPa and 1.15 ± 0.16 MPa after 1 day of immersion, respectively. The yield strength of the scaffolds was not observed to vary extensively with longer immersion periods. Where after 14 days of immersion, the Fe scaffolds exhibited 4.65 ± 0.09 MPa and the Fe-15AK scaffolds displayed a slight increase to 1.31 ± 0.15 MPa (**Figure 13e**). Furthermore, the ultimate compression strength (UCS) was determined for each sample (**Figure 13e**). Similar to the yield strength, the Fe and Fe-15AK groups displayed the highest and lowest UCS, respectively.

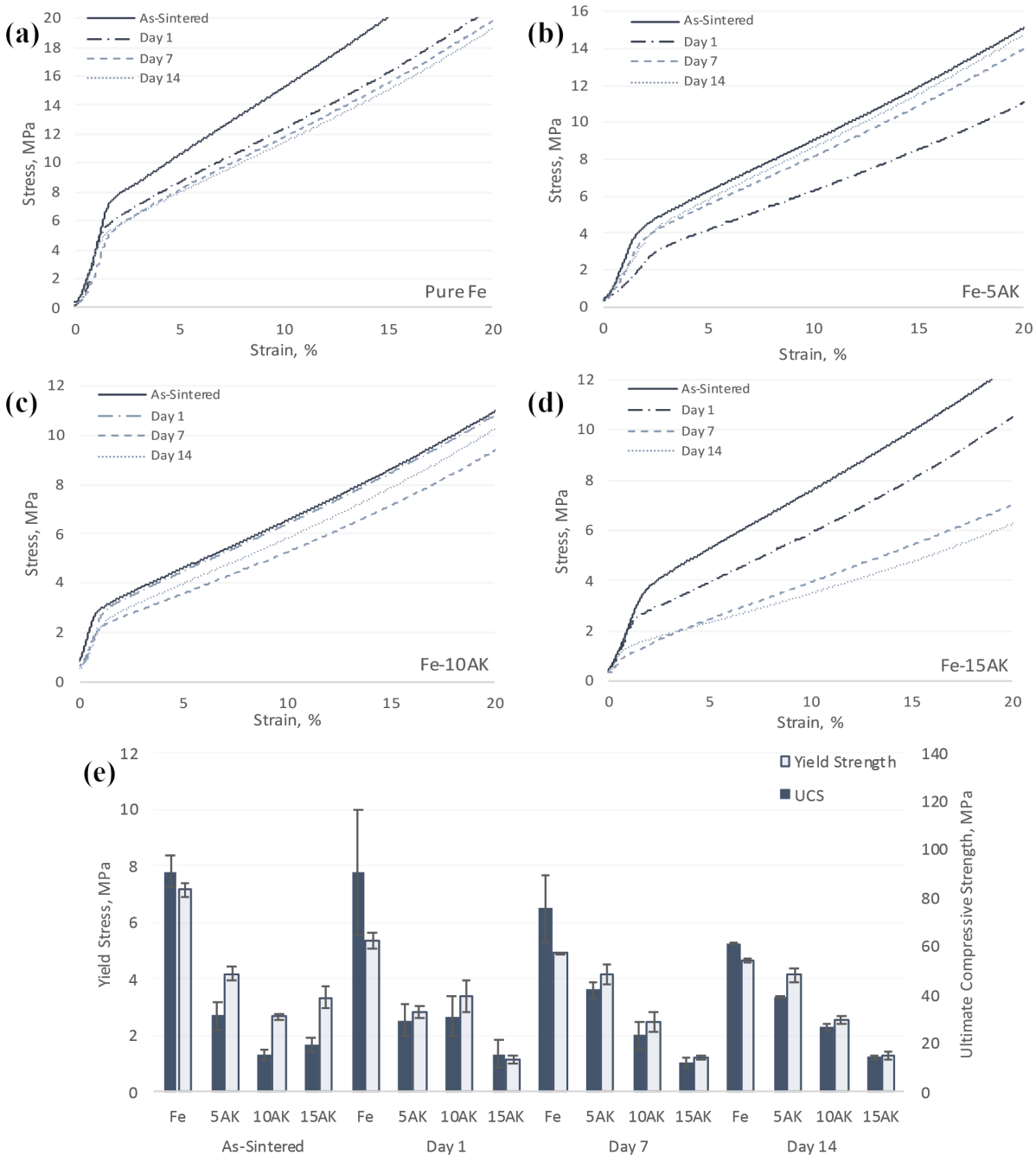


**Figure 13.** Stress-strain graphs of (a) pure Fe, (b) Fe-5AK, (c) Fe-10AK, (d) Fe-15AK and (e) yield strength and ultimate compressive strength of as-sintered and degrades samples.

## 3.4 Indirect cytocompatibility

The ion concentrations of the extract media derived from the Fe and Fe-AK scaffold are tabulated in **Table 5**. The α-MEM (without ascorbic acid, but with 10% FBS, 1% p/s) displayed the highest $PO_4$ and lowest Mg ion concentrations, 109.33 ppm and 19.83 ppm, respectively. The pure Fe-derived extract media exhibited the highest Fe ion concentration of 147.40 ppm. Whilst the Fe-AK scaffolds generated media with lower $PO_4$ and higher Mg and Si ion concentrations (**Table 5**). The Ca ion concentrations for all extract media ranged between 76.39 to 83.00 ppm. The indirect metabolic activity results are illustrated in **Figure 14**. After 1 day of culture, the preosteoblast MC3T3-E1 cells exhibited > 85% metabolic activity with every dilution of all samples. Where the 50% diluted Fe-15AK extract yielded the highest metabolic activity of 117.54 ± 14.68%, and the 100% pure Fe extract displayed the lowest activity of 87.93 ± 10.09%. After 3 days, the activity of the cells cultured within 100% extract media in all groups dropped below 40%. The recorded metabolic activity of all other dilutions was > 50%, except for the 75% pure Fe extract media. By 7 days of culture, the distinction between the 75% dilution of the Fe and Fe-AK extract media was more prominent, with metabolic activities of 36.98 ± 17.43% and ≥ 73.81%, respectively. Higher dilutions of the extract media only slightly inhibited the cell growth, with all sample groups exhibiting > 80% metabolic activity after 7 days.

## 3.5 Direct cytocompatibility

Directly seeding the preosteoblast cells to the scaffold surface resulted in a decrease in living cell count after 1 day. The pure Fe scaffolds produced the largest drop in viable cell count, 1.1 ± 0.2 ($x10^4$) cells (**Figure 14d**). The Fe-5AK and Fe-10AK yielded a relatively higher cell count after 1 day of culture, 1.5 ± 0.5 and 1.7 ± 0.2 ($x10^4$) cells, respectively. The Fe-15AK exhibited the highest viable cell count of 2.8 ± 0.4 ($x10^4$) cells. After 7 days, the viable cell count dropped further for all sample groups, retaining the trend where the pure Fe displayed the lowest (0.34 ± 0.02 ($x10^4$) cells) and Fe-15AK exhibited the highest living cell count (1.68 ± 0.08 ($x10^4$) cells). The cell count did not significantly reduce any further by the 14-day culture. Live/dead staining of the directly seeded preosteoblast cells depict the viable cells (green) on the surface of the scaffolds (**Figure 15**). Initially, more live cells were imaged on the Fe-AK scaffolds compared to the pure Fe scaffolds. This variation became more prominent with longer culture times, where the Fe-15AK scaffold showed the densest distribution of viable cells (**Figure 15d**). Conversely, after 14 days of culture, the Fe scaffold exhibited minimal viable cells (**Figure 15a**).

**Table 5.** Ion concentrations with extract media employed to assess indirect metabolic activity.

| *Sample* | *Fe (ppm)* | *$PO_4$ (ppm)* | *Ca (ppm)* | *Mg (ppm)* | *Si (ppm)* |
|---|---|---|---|---|---|
| *α-MEM* | / | 109.33 | 76.33 | 19.83 | / |
| *Pure Fe* | 147.40 | 93.24 | 76.29 | 20.74 | 0.51 |
| *Fe-5AK* | 34.59 | 83.88 | 83.00 | 27.14 | 35.62 |
| *Fe-10AK* | 23.92 | 80.61 | 77.35 | 29.91 | 53.57 |
| *Fe-15AK* | 38.49 | 79.60 | 77.49 | 37.72 | 96.57 |

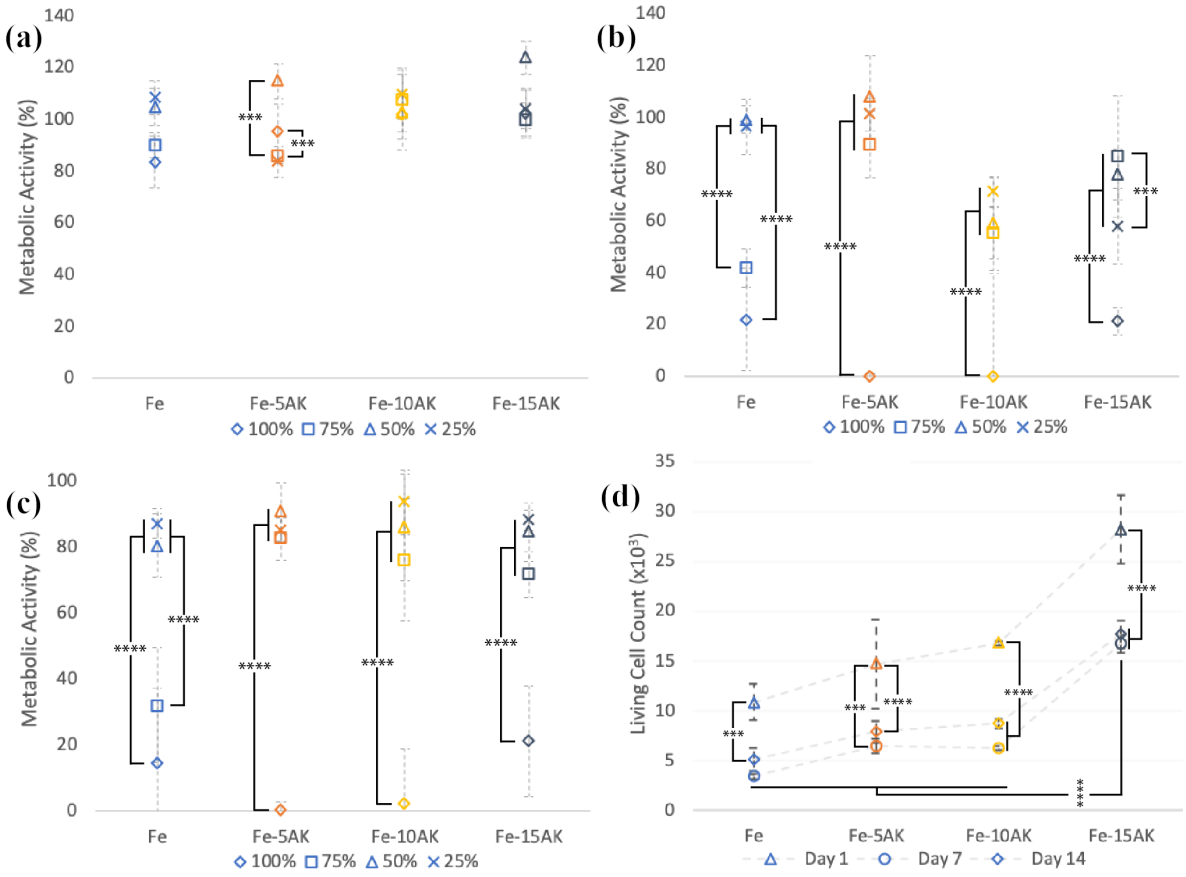


**Figure 14.** *In vitro* evaluation of Fe and Fe-AK scaffolds: indirect metabolic activity of MC3T3-E1 cell cultured in extract media after (a) 1-day, (b) 3-day (c) 7-day incubation and (d) direct cytotoxicity test cell count results (*** = $p$ <0.001 and **** = $p$ <0.0001).

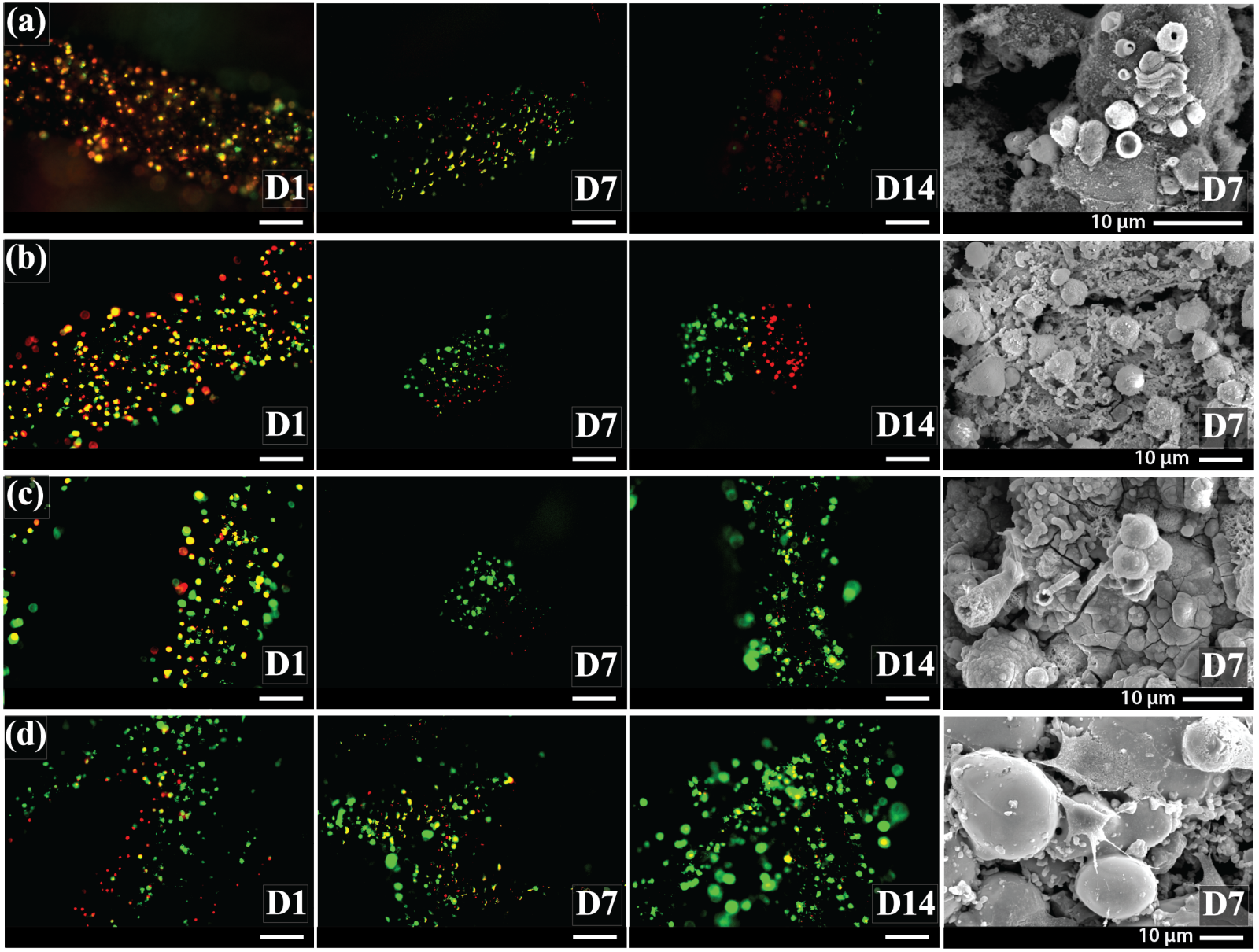


**Figure 15.** Direct cytotoxicity test: live/dead staining images (scale bar represents 100 µm) and morphology of fixed preosteoblast cells on (a) pure Fe, (b) Fe-5AK, (c) Fe-10AK and (d) Fe-15AK scaffold samples.

# 4 Discussion

This research comprised the fabrication and characterisation of extrusion-based AM of Fe-AK composite scaffolds. The addition of the AK bioceramic was employed primarily to increase the degradation rate and biocompatibility of the scaffold samples in orthopaedic applications. The results obtained indicated that the inclusion of AK increased the degradation rates of the overall scaffold without inducing brittle material behaviour. Furthermore, AK was also shown to improve osteoblastic cell metabolic activity and overall biocompatibility.

## 4.1 Fabrication and post-processing of 3D printed scaffolds

The extrusion-based AM and heat treatment yielded Fe and Fe-AK composite scaffolds that approximated the width, height and strut-width of the original design. Successful printing was observed with all the various Fe-based inks, where the printing pressure was the only variable that was altered, depending on the AK content of the ink. The different printing pressures are a direct result of the rheological properties of the inks. The slight increase in binder content between binder content of the Fe and Fe-AK inks, 51.02 and 52.55 vol%, served to decrease the overall viscosity. Additionally, two competing factors determined the change in shear-thinning of the inks, namely, the combination of small AK and large Fe particles, and the higher surface area of the AK particles. Combining particles of different sizes decreases viscosity due to the effect of polydispersity [45]. This effect is more pronounced with the Fe-5AK and Fe-10AK inks which exhibited lower viscosity relative to the pure Fe ink, thusly requiring lower printing pressures. On the other hand, the higher surface area could suggest that the AK particles are more hydrophilic relative to the Fe [46]. Though no article discusses the wettability of AK, water contact angles have been shown to decrease with other relevant bioceramics, including HA [34], $CaSiO_3$ [18] and diopside [47] surface coatings, *i.e.* more hydrophilic [47]. The viscosity of solutions containing suspended particles increases with particles that are more hydrophilic [46]. The latter may explain the increased viscosity noted with the Fe-15AK ink and subsequently, the increased printing pressure required. However, wettability analysis of AK is required to confirm this effect.

The average mass of the scaffold decreased with AK content due to the lower relative density of AK compared to Fe (**Table 3**). During the heat treatment, 3 - 4% shrinkage in diameter and height was noted for all sample groups. This shrinkage is a common occurrence when sintering powder-based components [9], [32], [37]. However, the observation of a relatively similar uniform shrinkage amongst all groups implies that the addition of AK did not impart sufficient thermal inhomogeneity to induce observable structural deformations. The absolute porosity of the scaffolds also increased with AK content (**Table 3**), a result of the fragmented morphology and higher microporosity of the AK powder. The microstructure of the Fe scaffolds encompassed partially sintered Fe particles (**Figure 4**) and the Fe-AK composite scaffolds contained partially sintered Fe and AK particles (**Figure 5-7**). Furthermore,

the fine distribution of Ca, Mg, Si and O detected on the surface of the AK containing samples (**Figure 5c, 6c and 7c**) is a result of the dissolution of AK in the water contained within the HPMC binder. This fine distribution could beneficially improve the osteointegration and osteoconductive characteristics of the scaffold by incorporating more biocompatible elements on the Fe surface [28], [33]. Additionally, this fine layer may enhance localised corrosion mechanisms, hastening degradation rates and generating a rougher surface that allows better cell adhesion.

Examinations of the scaffold cross-sections showed a matrix of partially fused particles (**Figure 5e, 6e, 7e**). The porous and AK area fractions increased with higher AK content (**Figure 3d**). Although the solid fraction could be increased by altering the heat treatment parameters, for example, sintering with an applied pressure [28], the inclusion of macro and microporosity may be beneficial in reducing the elastic modulus of the pure Fe to better match that of natural bone tissue [9]. Additionally, line EDS analysis on the sample cross-section indicated interdiffusion between the Fe and AK particles (**Figure 5f, 6f, 7f**). New crystalline phases were not detected (**Figure S2**) therefore suggesting that the Ca, Mg and Si ions dissolved into the adjacent Fe forming a solid solution. Such an effect is consistent with Fe-calcium silicate composites, where the difference in chemical composition could increase the potential for micro-galvanic and localised corrosion mechanisms [31].

## 4.2 Static *in-vitro* immersion

The degradation rates exhibited by the samples were observed to increase with higher AK content, with Fe-15AK displaying the highest mass loss of 12.4% (0.17 mm/year) after 14-day immersion. Sol-gel derived porous AK has been reported to exhibit 11% mass loss after 14-day immersion in Ringer's solution [48]. However, this result does not necessarily imply that the Fe-15AK scaffold displays superior degradation to pure AK as the different fabrication methods and immersion media will alter degradative properties. The closest analogous material that has been reported to date is extrusion-based AM Fe-30 (vol. %) $CaSiO_3$, exhibiting an ≈ 8% mass loss after 14 days of static immersion [32]. Other close analogous samples were powder metallurgy derived bulk Fe-50 (vol%) tricalcium phosphate (TCP) [28] and Fe- 1 (wt%) $Mg_2Si$ [30] which degraded at 0.18 and 0.19 mm/year, respectively. The pure Fe scaffold exhibited a degradation rate of 0.11 mm/year after 14-day immersion. This result resembles the observation reported in [9], where extrusion-based AM Fe degraded at 0.09 mm/year in r-SBF. Furthermore, this result falls within the degradation range of bulk powder metallurgy-derived Fe, 0.09 – 0.25 mm/year [17], [25], [28]–[30], though it should be noted that different immersion media were employed in the latter investigations, for example, NaCl or modified Hank's solution (**Table 6**).

After 1 day of immersion, the Fe-AK samples exhibited a high degradation rate that slowed down with longer immersion periods (**Table 4**). This effect was attributed to the dissolutive properties of AK, where the bioceramic rapidly dissolved in the immersion media during the initial period of immersion. This result was further verified by the relatively high Ca, Mg and Si ion concentrations

recorded from the immersion media of the Fe-AK samples (**Figure 12**). Additionally, the rapid dissolution of AK subsequently exposed a larger surface area of the Fe particles, further increasing the corrosion rate of the more dissolution resistant Fe. Similar observations were documented with Fe-bredigite composites [33].

The corrosion products developed during immersion comprised of Ca, Mg, Na, C, Cl, P and K were detected through EDS surface analysis. Potentially, these corrosion products formed as amorphous phases, undetectable by XRD which only recorded Fe and lepidocrocite on all degraded samples (**Figure S4**). The pure Fe scaffold initially developed Fe-, C- and O-containing corrosion phases. During immersion, an electrochemical reaction is generated between the corrosive media and the surface of the Fe [8]. As the electrochemical reaction progresses, positive Fe ions are released from the implant whilst simultaneously a cathodic release of hydroxide ions occurs. The Fe ions deposit as a weakly soluble porous iron hydroxide layer upon the surface of the active surface, as evident by the lepidocrocite detected through XRD [7], [8] (**Figure S4**). The Fe-, C- and O-based corrosion products noted after cleaning (**Figure S5**) could potentially be iron-carbonate based phases that are also known to form corrosion inhibitive surface layers [49], detailed further in **Section 4.3**. However, these layers do not completely hinder further corrosion as $Cl^-$ ions present in the r-SBF can react with this layer to form iron chlorides [27], [50], [51], indicated by the observed Cl-containing corrosion products (**Figure 8i, 10e**).

**Table 6** – *In vitro* degradation rates of Fe and Fe-ceramic composite materials

| ***Sample*** | ***Medium*** | ***Corrosion rate (mm/year)*** | ***Reference*** |
|---|---|---|---|
| *Fe-15AK (Porous)* | r-SBF | 0.17 | |
| *Fe-30 (vol%) $Ca_2SiO_4$ (Porous)* | Tris-HCl solution | 8 (Mass loss %) | [32] |
| *Pure AK (Porous)* | Ringer's solution | 11 (Mass loss %) | [38] |
| *Fe-50 (vol%) TCP* | NaCl solution | 0.18 | [28] |
| *Fe- 1 (wt%) $Mg_2Si$* | Modified Hanks Solution | 0.19 | [30] |
| *Pure Fe (Porous)* | r-SBF | 0.09 | [9] |
| *Pure Fe* | Kokubo's solution | 0.11 | [25] |
| *Pure Fe* | Modified Hanks Solution | 0.25 | [29] |
| *Pure Fe* | NaCl solution | 0.153 | [17] |

With longer degradation periods, Ca and $PO_4$ ions present in the r-SBF, precipitate on the porous iron hydroxide surface, as noted with pure Fe scaffolds after 7-day immersion (**Figure 8g**). The Fe-10AK scaffolds developed corrosion products that contained a Ca/P ratio of 2.27 (**Figure 10i**). (HA displays a Ca/P ratio of 1.67 [52]). Although HA was most likely not formed during the degradation of all samples, the precipitation of Ca and $PO_4$ has the potential to form apatitic phases and directly influence the mineralisation of forming bone. Moreover, the soluble AK will further increase the concentrations of osteogenic ions, *i.e.*, Ca, P, Mg and/or Si, into the surrounding fluid and accelerate surface mineralisation [17], [29], [31]. This effect was confirmed by the more rapid development of Ca-containing corrosion species with the Fe-10AK and Fe-15AK scaffolds (**Figure 10f, 11f**). The latter is ideal as bone cell adhesion, differentiation and proliferation then occur upon this apatite layer [27], [28], [33].

After 14 days of immersion, the Fe-AK groups developed a precipitated layer that contained Ca, Na, P and O and minimal Mg, similar to observations documented with Fe-bredigite composites [33]. Future research could investigate the macroenvironmental changes that occur during immersion, including pH and temperature monitoring. Similarly, the different structures that formed during immersion, namely the globular structures **(Figure 8d, 10f, and 11b, f**), rosette-like morphology (**Figure 8f, 9c, 10d**) and coral-like structures (**Figure 8i, 10e**) are also a result of micro-environmental characteristics. The rough and porous nature of the corrosion layer is further beneficial, offering the potential to improve cell adhesion. Furthermore, the rough and porous corrosion layer noted on day 14 of the degraded samples (**Figure 8h, 9h, 10g, 11h**) is similarly reported with degraded Fe-bredigite [21], Fe-HA and Fe-TCP [27] composites.

## 4.3 Mechanical characteristics

The mechanical properties of bulk Fe far exceed those of natural bone tissue, in terms of Young's modulus and yield strength, which is not ideal for orthopaedic implant applications as the mismatch in mechanical properties can lead to stress-shielding that deteriorates the quality of the surrounding bone tissue [7], [8]. The as-sintered Fe scaffold exhibited a yield strength of 7.15 ± 0.24 MPa, which agrees with pure Fe scaffolds investigated in [9]. The AK containing scaffolds exhibited a drop in compressive yield strength (**Figure 13e**). This trend can be attributed to the relatively poorer fusion between the Fe and AK particles and the high defect density inherent to ceramics [53]. However, even after 14-day immersion, all scaffolds exhibited a yield strength in the range of human trabecular bone, 0.2 – 80 MPa [54].

The mechanical integrity of the Fe and Fe-AK scaffolds is a dynamic characteristic that changes throughout the immersion period, where a drop in compressive yield strength after 1-day immersion was the common trend, a consequence of the mass loss due to corrosion. For the Fe-AK scaffolds, the variation in yield strength by day 1 was relatively larger due to the immediate dissolution of AK.

Prolonged immersion times did not induce as large a reduction in yield strength, potentially due to the dissolution resistant corrosion phases that did not get removed during the cleaning process (**Figure S5**). These phases are most likely iron carbonate-based, a common corrosion product generated during the degradation of Fe-based materials that are reported to form corrosion protective scales [49]. The corrosion products would reduce the rate of degradation during immersion as well as build up in the crevices of the scaffold and assist in supporting the applied loads. Consequently, minimising the change in yield strength with the longer immersion periods.

The retention of mechanical integrity is imperative for bone replacement applications, where the implant must retain sufficient strength and fracture toughness until the new bone tissue can support body loads. Furthermore, it should be noted that the stress-strain graphs of the Fe-AK composite scaffolds indicated permissible strains in excess of 20% before reaching the ultimate compressive stress, even after degradation (**Figure 13a-d**). This ideal result implies that additions of up to 15 vol% AK do not induce a drastic shift towards brittle material behaviour. Further investigations could be directed towards more extensive mechanical characterisation to better understand the dynamic material behaviour, potentially through impact testing, failure-mode analysis and corrosion fatigue analysis.

## 4.4 Cytocompatibility

ICP-OES analysis of the extract media (**Table 5**) used in the indirect cytocompatibility test followed similar trends as noted with the static immersion ion concentrations (**Figure 12**). The fresh α-MEM (without ascorbic acid, but with 10% FBS, 1% p/s) displayed the highest $PO_4$ ion concentration (109.33 ppm) that decreased with the Fe and Fe-AK extract media. This is a result of the $PO_4$ being consumed and precipitated as corrosion products on the scaffold surface. The pure Fe extract media displayed similar Ca and Mg ion concentrations to the fresh α-MEM whilst the Fe-AK extract media displayed incrementally increasing Mg ion concentrations, owing to the dissolution of AK into solution. The Ca ion concentrations were highest with the Fe-5AK extract media. The latter is further confirmation that Ca-containing phases form more rapidly on the Fe-10AK and Fe-15AK scaffolds, as observed with the static immersion tests (**Section 4.2**).

The metabolic activity of preosteoblast cells was directly affected by both the AK content of samples used to make the extract media and the dilution level of the extract media. The 100% extract media greatly hindered cell metabolic activity for all sample groups, defined by the ISO 10993-5 as severely toxic (level 4) [55]. The 75% Fe extract media also exhibited an inhibitory effect on the preosteoblast growth, displaying 36.98 ± 17.43% metabolic activity by day 7. Whilst, the 75% Fe-AK extract media slightly impeded cell growth, developing metabolic activities > 70%. Higher dilutions of the extract media of all groups displayed superior metabolic activity values, > 80% by day 7. Fe ions are known to induce the uncontrolled formation of reactive oxygen species (ROS) which in excessive amounts induce oxidative stress and harm the cells [9], [13]. The Fe-AK samples yielded extract fluid containing relatively less Fe ion concentrations and higher Ca, Mg and Si ion concentrations. Therefore,

less dilution of the extract media was required to retain adequate levels of metabolic activity. When considering *in-vivo* conditions, the dynamic flow of body fluids will reduce the localised ion concentrations [56], such that in practice higher dilutions of the extract media (*i.e.* 75%). may better resemble the surrounding body fluid. The improvement in cell viability is also noted with Fe-Pd-bredigite [21], Fe-HA and Fe-TCP [27] composite materials.

The results of the direct seeding cytocompatibility tests indicated that the pure Fe scaffold exhibited the most cytotoxic properties, displaying the lowest viable cell count for each culture period (**Figure 15**). The Fe-5AK and Fe-10AK scaffolds exhibited slightly higher viable cell counts, relative to the pure Fe scaffold. However, the Fe-15AK group displayed a statistically significant increase in viable cell count relative to all other sample groups. From the *in vitro* immersion testing, it was noted that the AK addition to the scaffold induced more rapid degradation and hastened the formation of Ca- and Na-containing corrosion products. These products more closely resemble the chemistry of natural apatite, improving osteoblast adhesion and proliferation [57]. Moreover, the rough and porous nature of the corrosion layer is known to further improve osteointegration, similar to investigations discussing highly porous HA-coated Fe [58] and Fe-TCP substrates [34]. Therefore, the addition of 15 vol% AK, and the subsequent increase in bone-forming ions and more rapid formation of corrosion products, significantly reduce the cytotoxic effects observed from the pure Fe equivalents. *In vitro* cytocompatibility tests do not perfectly simulate *in vivo* conditions, and based on the preliminary results obtained, further analysis towards *in vivo* studies on AM-derived Fe-AK scaffolds are justified.

# 5 Conclusion

To summarise, Fe-akermanite scaffolds were successfully fabricated through extrusion-based additive manufacturing and heat treatment. The technique allowed for the design of reticulated geometry and the incorporation of random micropores on the surface. The addition of AK to the scaffold significantly altered the overall degradation characteristics, with the 15 vol% addition of AK inducing a 64.7% increase in degradation rate after 14 days of immersion, 0.17 mm/year compared to the 0.11 mm/year of pure Fe. Furthermore, the higher ion concentrations in the immersion media hastened the development of corrosion products containing bone-forming elements. The mechanical properties of the scaffolds were certainly affected by the addition of AK, where the Fe-AK scaffolds displayed reduced yield strength compared the that of the pure Fe. After 14-day immersion, the Fe-15AK exhibited the lowest yield strength of 1.31 MPa. However, all sample groups, even after degradation, retained a yield strength within the range of trabecular bone. The ductile-like material behaviour of Fe-AK scaffolds, indicated by the stress-strain graphs, implies that the AK addition did not impart brittle-like material characteristics, and is additionally ideal for bone replacement applications. Furthermore, cytocompatibility characterisation of the Fe-AK scaffolds has indicated that the addition of AK directly improves preosteoblast metabolic activity and proliferation. Where even just a 5 vol% AK addition was sufficient to improve the preosteoblast metabolic activity during indirect cytocompatibility analysis. The Fe-15AK displayed a statistically significant improvement during direct cytocompatibility assessment. Ultimately, the Fe-15AK sample group displayed the best overall degradation and cytocompatibility characteristics and adequate mechanical properties for bone substitution applications.

# 6 Future Works

Future research should be directed towards better defining the long-term degradation characteristics of the composite scaffolds, potentially through longer immersion periods whilst monitoring the pH variations and possibly introducing a dynamic immersion setup to better mimic the *in vivo* environment. Dynamic mechanical testing such as corrosion fatigue and impact testing would also be useful to more precisely define the material failure-mode and mechanical characteristics. Furthermore, differentiation cell tests can be performed to better estimate the *in vivo* performance of the composite samples. Finally, the issue regarding the ferromagnetic properties displayed by the Fe content of the samples is yet to be addressed, possibly through the incorporation of Mn alloying elements [12], [59].

# 7 References


[1] Y. Du, J. L. Guo, J. Wang, A. G. Mikos, and S. Zhang, "Hierarchically designed bone scaffolds: From internal cues to external stimuli," *Biomaterials*, vol. 218, p. 119334, 2019.

[2] C. Wolf-Brandstetter and D. Scharnweber, "Biocomposite and Bioceramic Coatings and Materials," in *Handbook of Nanoceramic and Nanocomposite Coatings and Materials*, Elsevier Ltd., 445-470, 2015, pp. 445–470.

[3] R. Wu *et al.*, "Bone tissue regeneration: The role of finely tuned pore architecture of bioactive scaffolds before clinical translation," *Bioact. Mater.*, vol. 6, no. 5, pp. 1242–1254, 2021.

[4] T. Albrektsson and C. Johansson, "Osteoinduction, osteoconduction and osseointegration," *Eur. Spine J.*, vol. 10, pp. S96–S101, 2001.

[5] E. H. Schemitsch, "Size Matters: Defining Critical in Bone Defect Size!," *J. Orthop. Trauma*, vol. 31, no. 10, pp. S20–S22, 2017.

[6] F. Witte and A. Eliezer, "Biodegradable metals," *Degrad. Implant Mater.*, vol. 9781461439, pp. 93–109, 2012.

[7] R. Gorejová, L. Haverová, R. Oriňaková, A. Oriňak, and M. Oriňak, "Recent advancements in Fe-based biodegradable materials for bone repair," *J. Mater. Sci.*, vol. 54, no. 3, pp. 1913–1947, 2019.

[8] J. He *et al.*, "Advances in Fe-based biodegradable metallic materials," *RSC Adv.*, vol. 6, no. 114, pp. 112819–112838, 2016.

[9] N. E. Putra *et al.*, "Extrusion-based 3D printed biodegradable porous iron," *Acta Biomater.*, vol. 121, pp. 741–756, 2020.

[10] P. Sharma, K. G. Jain, P. M. Pandey, and S. Mohanty, "In vitro degradation behaviour, cytocompatibility and hemocompatibility of topologically ordered porous iron scaffold prepared using 3D printing and pressureless microwave sintering," *Mater. Sci. Eng. C*, vol. 106, no. September 2019, p. 110247, 2020.

[11] H. Li, Y. Zheng, and L. Qin, "Progress of biodegradable metals," *Prog. Nat. Sci. Mater. Int.*, vol. 24, no. 5, pp. 414–422, 2014.

[12] D. Carluccio *et al.*, "Additively manufactured iron-manganese for biodegradable porous load-bearing bone scaffold applications," *Acta Biomater.*, vol. 103, pp. 346–360, 2020.

[13] R. Eid, N. T. T. Arab, and M. T. Greenwood, "Iron mediated toxicity and programmed cell death: A review and a re-examination of existing paradigms," *Biochimica et Biophysica Acta - Molecular Cell Research*, vol. 1864, no. 2. Elsevier B.V., pp. 399–430, 01-Feb-2017.

[14] J. Alvarado, R. Maldonado, J. Marxuach, and R. Otero, "Biomechanics of hip and knee protheses," *Appl. Eng. Mech. Med. GED*, pp. 6–22, 2003.

[15] Y. Leng *et al.*, "Material-based therapy for bone nonunion," *Mater. Des.*, vol. 183, p. 108161, 2019.

[16] M. P. Nikolova and M. S. Chavali, “Recent advances in biomaterials for 3D scaffolds: A review,” *Bioact. Mater.*, vol. 4, no. October, pp. 271–292, 2019.

[17] A. Reindl, R. Borowsky, S. B. Hein, J. Geis-Gerstorfer, P. Imgrund, and F. Petzoldt, “Degradation behavior of novel Fe/ß-TCP composites produced by powder injection molding for cortical bone replacement,” *J. Mater. Sci.*, vol. 49, no. 24, pp. 8234–8243, 2014.

[18] C. Shuai *et al.*, “Fabricating the nanostructured surfaces of CaSiO3 scaffolds,” *Appl. Surf. Sci.*, vol. 455, pp. 1150–1160, 2018.

[19] W. Zhen *et al.*, “Role of the porous structure of the bioceramic scaffolds in bone tissue engineering,” *Nat. Preced.*, 2010.

[20] J. Liu *et al.*, “Bioinspired scaffolds with hierarchical structures for tailored mechanical behaviour and cell migration,” *Ceram. Int.*, vol. 46, no. 15, pp. 24102–24109, 2020.

[21] C. Gao, M. Yao, S. Li, P. Feng, S. Peng, and C. Shuai, “Highly biodegradable and bioactive Fe-Pd-bredigite biocomposites prepared by selective laser melting,” *J. Adv. Res.*, vol. 20, pp. 91–104, 2019.

[22] Z. Wen, L. Zhang, C. Chen, Y. Liu, C. Wu, and C. Dai, “A construction of novel iron-foam-based calcium phosphate/chitosan coating biodegradable scaffold material,” *Mater. Sci. Eng. C*, vol. 33, no. 3, pp. 1022–1031, 2013.

[23] N. R. and P. P. G. Patel, “‘A Review on Biomaterials : Scope , Applications & Human Anatomy Significance.,’” vol. 2, no. 4, pp. 91–101, 2012.

[24] M. Sikora-Jasinska, E. Mostaed, A. Mostaed, R. Beanland, D. Mantovani, and M. Vedani, “Fabrication, mechanical properties and in vitro degradation behavior of newly developed Zn-Ag alloys for degradable implant applications,” *Mater. Sci. Eng. C*, vol. 77, pp. 1170–1181, 2017.

[25] M. Dehestani, E. Adolfsson, and L. A. Stanciu, “Mechanical properties and corrosion behavior of powder metallurgy iron-hydroxyapatite composites for biodegradable implant applications,” *Mater. Des.*, vol. 109, pp. 556–569, 2016.

[26] J. A. Nordin, D. H. Prajitno, S. Saidin, H. Nur, and H. Hermawan, “Structure-property relationships of iron-hydroxyapatite ceramic matrix nanocomposite fabricated using mechanosynthesis method,” *Mater. Sci. Eng. C*, vol. 51, pp. 294–299, 2015.

[27] M. F. Ulum *et al.*, “In vitro and in vivo degradation evaluation of novel iron-bioceramic composites for bone implant applications,” *Mater. Sci. Eng. C*, vol. 36, no. 1, pp. 336–344, 2014.

[28] E. B. Montufar *et al.*, “High strength, biodegradable and cytocompatible alpha tricalcium phosphate-iron composites for temporal reduction of bone fractures,” *Acta Biomater.*, vol. 70, pp. 293–303, 2018.

[29] M. Sikora-Jasinska *et al.*, “Synthesis, mechanical properties and corrosion behavior of powder metallurgy processed Fe/Mg2Si composites for biodegradable implant applications,” *Mater. Sci. Eng. C*, vol. 81, no. July, pp. 511–521, 2017.

[30] M. Sikora-Jasinska *et al.*, "Long-term in vitro degradation behaviour of Fe and Fe/Mg2Si composites for biodegradable implant applications," *RSC Adv.*, vol. 8, no. 18, pp. 9627–9639, 2018.

[31] S. Wang, Y. Xu, J. Zhou, H. Li, J. Chang, and Z. Huan, "In vitro degradation and surface bioactivity of iron-matrix composites containing silicate-based bioceramic," *Bioact. Mater.*, vol. 2, no. 1, pp. 10–18, 2017.

[32] H. Ma *et al.*, "3D printing of high-strength bioscaffolds for the synergistic treatment of bone cancer," *NPG Asia Mater.*, vol. 10, no. 4, pp. 31–44, 2018.

[33] C. Shuai *et al.*, "Bioceramic enhances the degradation and bioactivity of iron bone implant," *Mater. Res. Express*, vol. 6, no. 115401, 2019.

[34] M. A. Surmeneva *et al.*, "Nano-hydroxyapatite-coated metal-ceramic composite of iron-tricalcium phosphate: Improving the surface wettability, adhesion and proliferation of mesenchymal stem cells in vitro," *Colloids Surfaces B Biointerfaces*, vol. 135, pp. 386–393, 2015.

[35] N. E. Putra, M. J. Mirzaali, I. Apachitei, J. Zhou, and A. A. Zadpoor, "Multi-material additive manufacturing technologies for Ti-, Mg-, and Fe-based biomaterials for bone substitution," *Acta Biomater.*, vol. 109, pp. 1–20, 2020.

[36] Y. Li *et al.*, "Additively manufactured biodegradable porous iron," *Acta Biomater.*, vol. 77, pp. 380–393, 2018.

[37] A. Mostafaei *et al.*, "Binder jet 3D printing – Process parameters, materials, properties, and challenges," *Prog. Mater. Sci.*, no. June, p. 100707, 2020.

[38] C. Wu and J. Chang, "Akermanite , and Bredigite Ceramics," *J. Biomed. Mater. Res.*, pp. 153–160, 2007.

[39] A. Khandan, M. Abdellahi, R. V. Barenji, N. Ozada, and E. Karamian, "Introducing natural hydroxyapatite-diopside (NHA-Di) nano-bioceramic coating," *Ceram. Int.*, vol. 41, no. 9, pp. 12355–12363, 2015.

[40] R. Density and L. P. Prod-, "Standard Test Methods for Oil Content , Oil-Impregnation Efficiency , and Surface- Connected Porosity of Sintered Powder Metallurgy ( PM ) Products Using Archimedes ' Principle 1," pp. 1–6, 2014.

[41] A. Oyane, H. Kim, T. Furuya, T. Kokubo, T. Miyazaki, and T. Nakamura, "J Biomed Mater Res 65A (2003) 188-195.pdf," pp. 19–21, 2002.

[42] ASTM International, "ASTM G1 - 03(2011) Standard Practice for Preparing, Cleaning, and Evaluating Corrosion Test Specimens," 2017.

[43] ASTM International, "ASTM G31 - 72(2004) Standard Practice for Laboratory Immersion Corrosion Testing of Metals," 2004.

[44] "ISO - ISO 13314:2011 - Mechanical testing of metals — Ductility testing — Compression test for porous and cellular metals." [Online]. Available: https://www.iso.org/standard/53669.html.

[Accessed: 18-May-2021].

[45] "Changing the Properties of Particles to Control Their Rheology." [Online]. Available: https://www.azom.com/article.aspx?ArticleID=12304. [Accessed: 08-Jul-2021].

[46] S. Alves, M. R. Alcantara, and A. M. Figueiredo Neto, "The effect of hydrophobic and hydrophilic fumed silica on the rheology of magnetorheological suspensions," *J. Rheol. (N. Y. N. Y).*, vol. 53, no. 3, pp. 651–662, 2009.

[47] A. Khandan, M. Abdellahi, N. Ozada, and H. Ghayour, "Study of the bioactivity, wettability and hardness behaviour of the bovine hydroxyapatite-diopside bio-nanocomposite coating," *J. Taiwan Inst. Chem. Eng.*, vol. 60, pp. 538–546, 2016.

[48] C. Wu, J. Chang, W. Zhai, S. Ni, and J. Wang, "Porous Akermanite Scaffolds for Bone Tissue Engineering: Preparation, Characterization, and In Vitro Studies," *Wiley Intersci.*, pp. 47–55, 2005.

[49] M. H. Sk *et al.*, "Local supersaturation and the growth of protective scales during CO2 corrosion of steel: Effect of pH and solution flow," *Corros. Sci.*, vol. 126, pp. 26–36, Sep. 2017.

[50] P. Sharma and P. M. Pandey, "Corrosion rate modelling of biodegradable porous iron scaffold considering the effect of porosity and pore morphology," *Mater. Sci. Eng. C*, vol. 103, no. February, p. 109776, 2019.

[51] H. Hermawan, "Updates on the research and development of absorbable metals for biomedical applications," *Prog. Biomater.*, vol. 7, no. 2, pp. 93–110, 2018.

[52] Elliot J. C., "Structure and Chemistry of the Apatites and Other Calcium Orthophosphates - J.C. Elliott - Google Libros," pp. 63–230, 1994.

[53] L. L. Hench, "Bioceramics," *Biomech. Biomater. Orthop. Second Ed.*, vol. 28, pp. 21–33, 2016.

[54] T. M. Keaveny, E. F. Morgan, G. L. Niebur, and O. C. Yeh, "Biomechanics of Trabecular Bone," *http://dx.doi.org/10.1146/annurev.bioeng.3.1.307*, vol. 3, pp. 307–333, Nov. 2003.

[55] ISO/ASTM, "ISO 10993-5:2009 - Biological evaluation of medical devices — Part 5: Tests for in vitro cytotoxicity." [Online]. Available: https://www.iso.org/standard/36406.html. [Accessed: 05-Jul-2021].

[56] M. F. Ulum *et al.*, "Evidences of in vivo bioactivity of Fe-bioceramic composites for temporary bone implants," *J. Biomed. Mater. Res. - Part B Appl. Biomater.*, vol. 103, no. 7, pp. 1354–1365, 2015.

[57] M. Caligari Conti *et al.*, "Optimisation of fluorapatite coating synthesis applied to a biodegradable substrate," *Surf. Eng.*, vol. 0, no. 0, pp. 1–11, 2018.

[58] C. Yang, Z. Huan, X. Wang, C. Wu, and J. Chang, "3D Printed Fe Scaffolds with HA Nanocoating for Bone Regeneration," *ACS Biomater. Sci. Eng.*, vol. 4, no. 2, pp. 608–616, 2018.

[59] J. Venezuela and M. S. Dargusch, "Addressing the slow corrosion rate of biodegradable Fe-Mn: Current approaches and future trends," *Curr. Opin. Solid State Mater. Sci.*, vol. 24, no. 3, p. 100822, 2020.

# 8 Supplementary Data

Theoretical density calculation:

$$\rho_{powder} = \frac{\%Fe.\rho_{Fe} + \%AK.\rho_{AK}}{100} \quad \textbf{(Equation S1)}$$

Where $\rho_{powder}$ is the theoretical density of the mixed powder (g/cm$^3$), %Fe and %AK represent the Fe and AK in the mixture (vol.%), $\rho_{Fe}$ is the theoretical density of iron (7.87 g/cm$^3$) and $\rho_{AK}$ is the theoretical density of akermanite (2.94 g/cm$^3$)

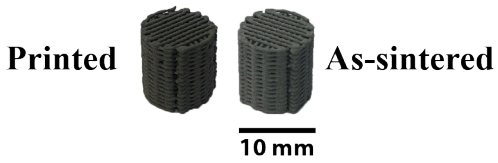


**Figure S1.** – Visual inspection of as-printed and as-sintered Fe-AK scaffolds.

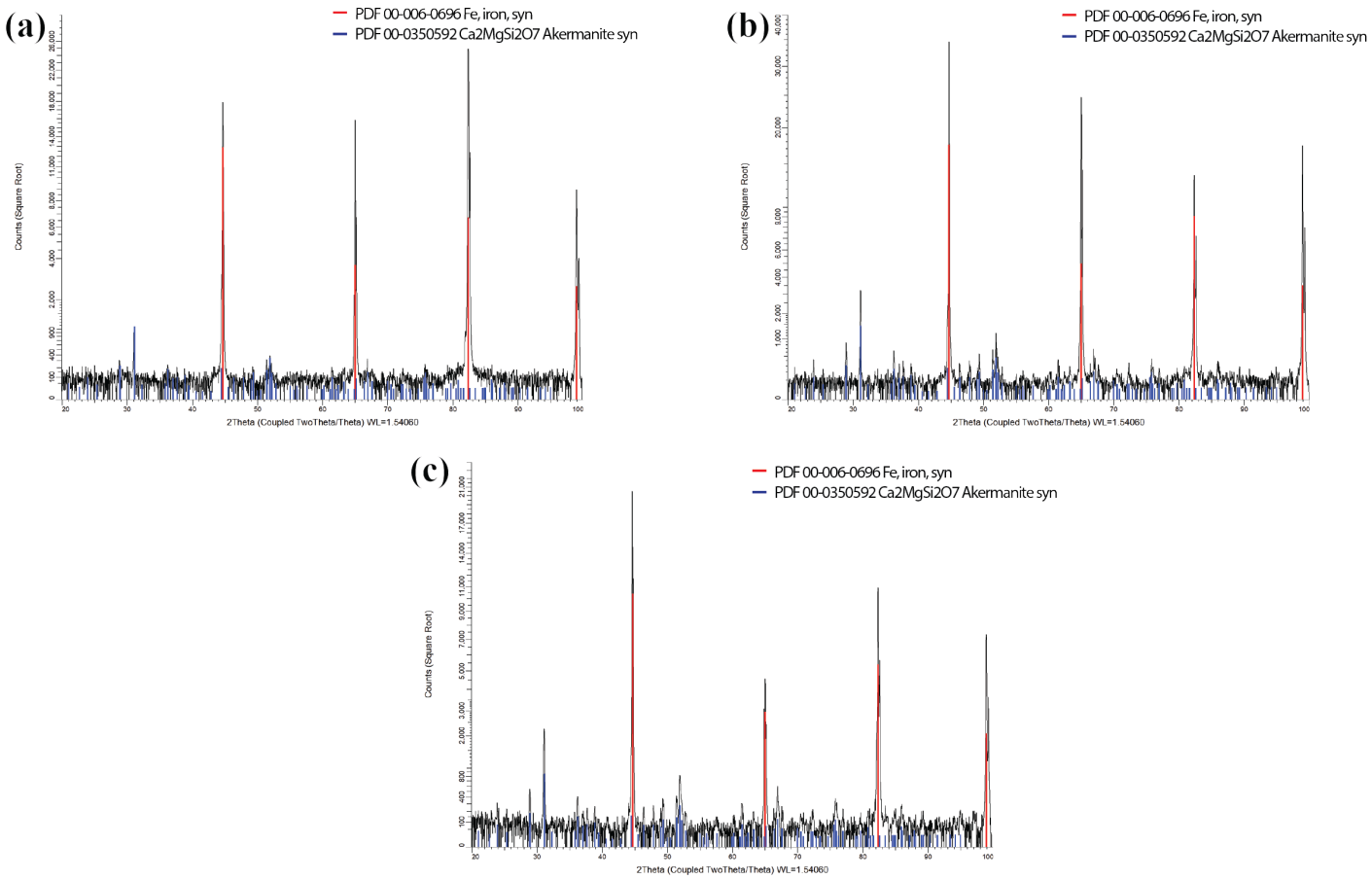


**Figure S2** – Diffractograms of as-sintered (a) Fe-5AK, (b) Fe-10AK and (c) Fe-15AK scaffolds.

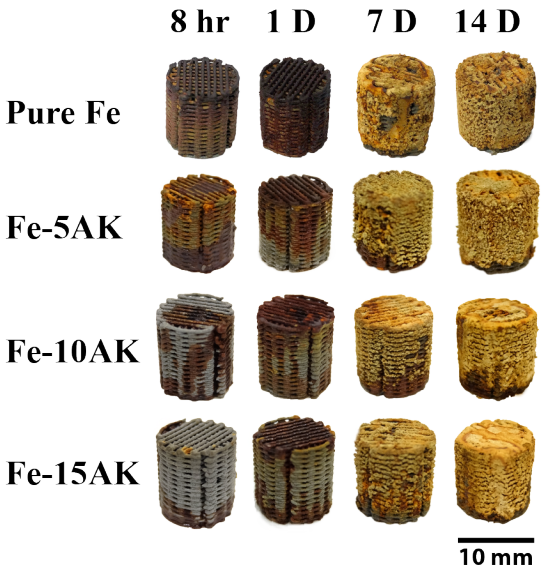


**Figure S3.** – Visual inspection of the biodegraded Fe-AK scaffolds specimens.

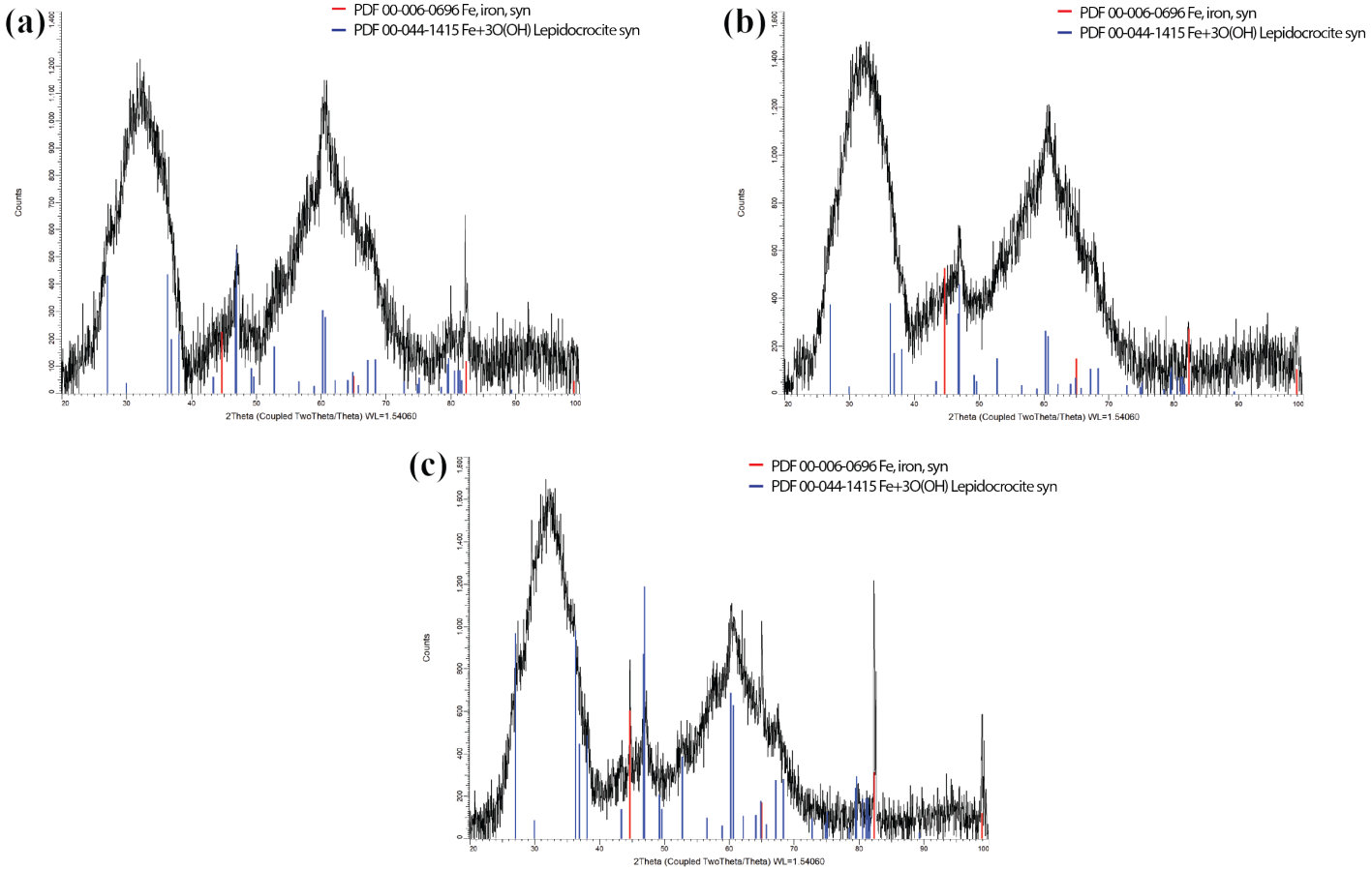


**Figure S4** – Diffractograms of (a) Fe-5AK, (b) Fe-10AK and (c) Fe-15AK scaffolds after 14 Day *in vitro* immersion.

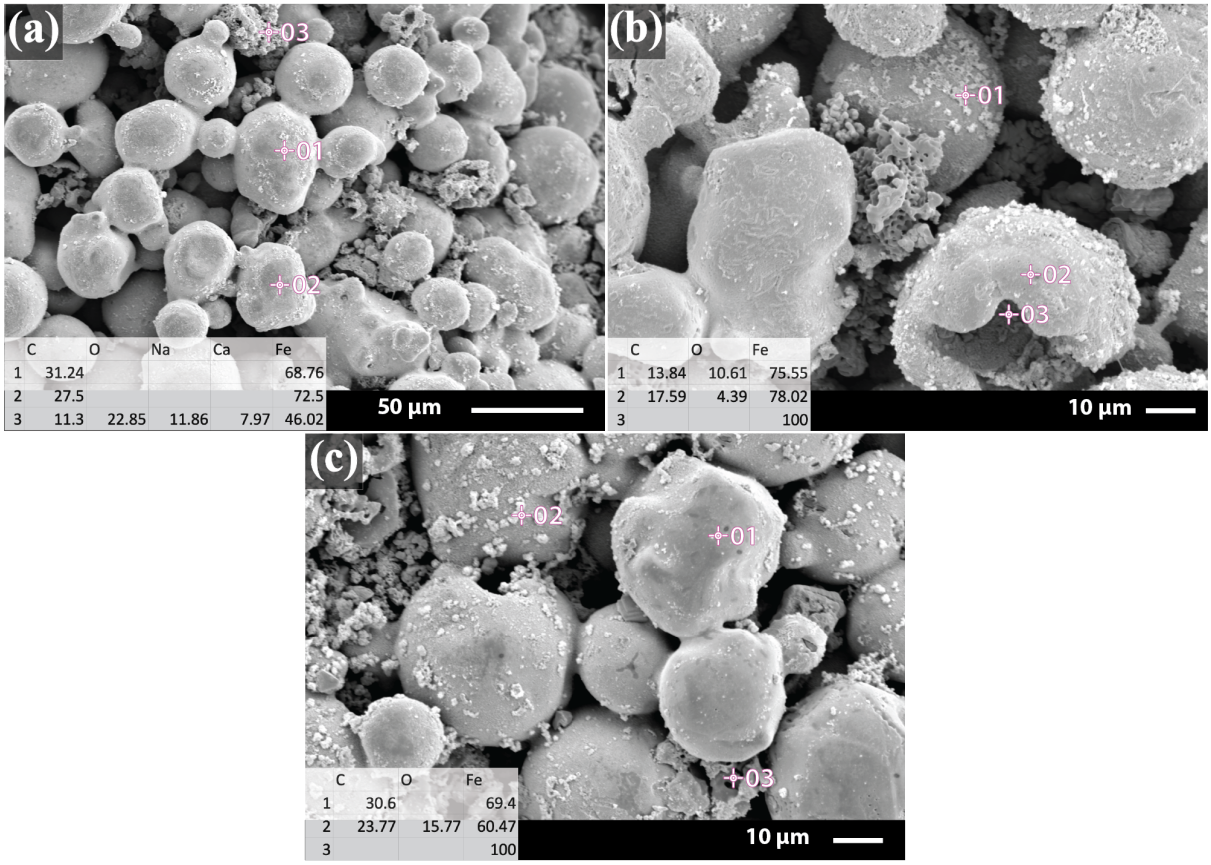


**Figure S5.** – EDS measurements of degraded scaffolds after cleaning; (a) Fe-5AK day 7, (b) Fe-10AK day 14, (c) Fe-15AK day 7